CDDpress

www.nature.com/cdd

ARTICLE OPEN

Check for updates

EGFR deletion in myeloid cells reprograms the immunosuppressive landscape of colorectal cancer

Ourania Fari[1,2,7], Angelika Neuhofer[1,2,7], Martin Holcmann[1,2], Tatiana Chontorotzea[1,2], Iros Barozzi[1,2], Thomas Mohr[1,2], Bernadette Blauensteiner[1,2], Dana Krauß[1,2], Yu-Tian Xiao[1,2], Michaela Lang[3], Dario L. Frey[4,5], Barbara Helm[4,5], Ursula Klingmüller[4,5], Matthias Farlik[2,6] and Maria Sibilia[1,2]✉

© The Author(s) 2026

Despite advances in the treatment of metastatic colorectal cancer (mCRC), it remains the second leading cause of cancer-related mortality, with limited effective therapeutic options. While EGFR inhibition is a standard first-line therapy for mCRC patients lacking *KRAS* mutations, resistance frequently develops, limiting its clinical benefit. Murine CRC models have shown that EGFR deletion in myeloid cells reduces tumor burden, and the presence of EGFR-positive myeloid cells is associated with poor prognosis in mCRC patients. However, the role of these cells in the therapeutic response to anti-EGFR therapies remains poorly understood. In this study, we integrated mouse models, single-cell RNA sequencing (scRNAseq), proteomics, and patient-derived mCRC datasets to investigate how EGFR signaling in myeloid cells shapes the tumor microenvironment (TME). In a preclinical therapeutic trial, we demonstrate that EGFR deletion in myeloid cells of tumor-bearing CRC mice reduced tumor growth, whereas EGFR loss in intestinal epithelial tumor cells alone had no therapeutic impact. EGFR deletion also decreased the abundance of F4/80^{hi} macrophages, particularly the Spp1^{+} and C1qc^{+} subsets, and reduced inflammatory pathways like TGFβ, IFNγ, and JAK/STAT signaling in myeloid cells. These changes altered myeloid–T cell interactions, resulting in a less immunosuppressive TME characterized by reduced immune checkpoint expression. Furthermore, we identified thrombospondin-1 (THBS1) as a myeloid-derived ligand interacting with T cells, and confirmed its regulation by EGFR signaling through proteomic analysis. Analysis of human CRC datasets revealed that high EGFR and THBS1 expression correlates with poor patient outcomes. Collectively, these findings establish EGFR signaling in myeloid cells as a critical regulator of the immunosuppressive TME and suggest that targeting EGFR within specific myeloid subsets could represent a promising therapeutic strategy in mCRC.

Cell Death & Differentiation; https://doi.org/10.1038/s41418-026-01774-x

INTRODUCTION

Colorectal cancer (CRC) is the second most common cause of cancer-related deaths. In recent years, incidence rates in the overall population have decreased, despite an increase among younger people [1, 2]. CRC originates in crypts, most frequently with an adenoma emergence after the loss of the *APC* gene, followed by adenocarcinoma development that coincides with the loss of *TP53*, while in case of invasive disease activating *KRAS* mutations occur [3]. Besides genetic alterations, environmental factors such as diet and smoking or inflammatory conditions have also been linked to the development of CRC. Specifically, inflammatory bowel disease is a risk factor for colitis-associated colorectal cancer (CAC) development, highlighting the connection between chronic inflammation and tumorigenesis [4].

Conventional CRC treatments usually include surgical resection combined with chemotherapy and/or radiotherapy for early stages (I-III) [5]. First-line treatment for metastatic patients with wild-type *KRAS/BRAF* employs chemotherapy in combination with epidermal growth factor receptor (EGFR)-blocking antibodies, whereas patients with mutant *KRAS/BRAF* are resistant to this treatment and receive chemotherapy combined with angiogenic inhibition (anti-VEGFA antibodies) [6]. However, among the patients with wild-type *KRAS/BRAF* and thus eligible for anti-EGFR therapies, a relatively high fraction does not respond, for reasons that are still unknown.

EGFR is a receptor tyrosine kinase that can be found dysregulated in a variety of epithelial cancers [7]. In recent years, however, EGFR has been associated with a tumor-promoting role when expressed by myeloid cells infiltrating colorectal tumors and hepatocellular carcinoma (HCC) [8, 9]. In genetically engineered mouse models (GEMMs), constitutive deletion of *Egfr*, specifically in myeloid cells before tumor initiation, led to reduced tumor burden in CRC and HCC, whereas EGFR deletion in tumor cells (intestinal epithelial cells and hepatocytes) did not affect (CRC) or even enhanced (HCC) tumor growth [8, 9]. Most importantly, EGFR-positive myeloid cells were also found in human CRC and HCC patients, and their presence correlated with reduced disease-free and overall survival [8, 9].

[1]Center for Cancer Research, Medical University of Vienna, Vienna, Austria. [2]Comprehensive Cancer Center, Medical University & General Hospital, Vienna, Austria. [3]Division of Gastroenterology and Hepatology, Department of Medicine 3, Medical University of Vienna, Vienna, Austria. [4]Division Systems Biology of Signal Transduction, German Cancer Research Center (DKFZ), Heidelberg, Germany. [5]Translational Lung Research Center (TLRC), German Center for Lung Research (DZL), Heidelberg, Germany. [6]Department of Dermatology, Medical University of Vienna, Vienna, Austria. [7]These authors contributed equally: Ourania Fari, Angelika Neuhofer. ✉email: maria.sibilia@meduniwien.ac.at

Received: 9 July 2025 Revised: 29 April 2026 Accepted: 20 May 2026
Published online: 02 June 2026

Tumor promotion was linked to cytokines derived from EGFR-positive myeloid populations, such as interleukin (IL) 6 and IL1β [8–10]. In a preclinical therapeutic trial where EGFR was deleted in intestinal tumor cells of GEMMs with established CRC, no tumor shrinkage was observed [8]. This raises the question of whether the efficacy of anti-EGFR therapies in CRC patients depends on EGFR inhibition in tumor cells, myeloid cells, or both.

Tumor-associated myeloid cells represent a heterogeneous population in solid tumors that can acquire different activation states to support or suppress tumor growth. Single-cell technologies are important tools to characterize and identify cell diversity and different phenotypes within tumors. In recent years, the presence of tumor-associated macrophages (TAMs) expressing markers such as *C1QC* or *SPP1* in human colorectal tumors has drawn a lot of attention as they were shown to have a tumor-promoting role. Some reports also show that the increased presence of *SPP1*-expressing TAMs correlates with a worse outcome for CRC patients [11, 12]. Monocytes marked by the expression of *CHIL3* have also been described as tumor-promoting [13].

Lymphoid cells and their activation states also play an important role in tumors. In CRC, several different T cell subsets and phenotypes have been described through single-cell technologies, which allow the detection of markers linked to naïve, activated, resting, exhausted, or regulatory states [14, 15]. It is important to understand how myeloid populations affect tumor growth directly or indirectly by modulating the migration, differentiation, and activation of other immune cells of the TME, such as T cells or natural killer (NK) cells. In this context, it is important to clarify the role of EGFR expression in tumor-associated myeloid cells in CRC. It remains unknown which myeloid cell population expresses EGFR and how this influences tumor cells and the surrounding microenvironment.

In this study, we show in a preclinical therapeutic trial that inducible deletion of EGFR in myeloid cells of GEMMs with established CRC results in tumor reduction, indicating that the therapeutic efficacy of EGFR inhibition largely relies on its action on myeloid cells. To investigate the resulting cellular activities in CRC upon deletion of EGFR in the myeloid compartment, we performed high-throughput single-cell RNA sequencing (scRNA-seq). We mined this newly generated data to predict whether and how EGFR expression in myeloid cells might affect TME composition and cell-cell communication within the TME of CRC. The resulting cell atlas formed the basis of a communication map that revealed candidate receptor-ligand pairs involved in the cross-talk between myeloid and T cells of the TME. We also evaluated EGFR-dependent alterations of gene expression at the protein level through mass spectrometry-based proteomic analysis of sorted myeloid populations. Further, we used a human CRC single-cell dataset to compare and validate our findings in human myeloid cells with low and high EGFR gene signatures and identified *EGFR* and *thrombospondin-1* (*THBS1*) co-expression as prognostic markers for tumor progression in human CRC. Taken together, our study enhances our understanding of EGFR-dependent gene regulatory circuits in myeloid cells, revealing alterations in their phenotype with possible consequences on the cross-talk between the different components within the TME.

RESULTS

EGFR deletion in myeloid cells of established CRC leads to reduced tumor burden

We have previously observed reduced tumor growth in mice constitutively lacking EGFR in myeloid cells ($Egfr^{\Delta MyI}$), whereas lack of EGFR in intestinal epithelial cells had no impact on tumor growth [8]. To investigate whether, in a therapeutic setting, EGFR inhibition in myeloid cells would lead to tumor regression, we used the tamoxifen-inducible *LysM-CreER*^{T2} mouse line to delete EGFR specifically in myeloid cells ($Egfr^{\Delta MyI\text{-}ER}$) of already established AOM/DSS-induced colorectal tumors (Fig. 1A). Recombination and reduced expression of *Egfr* upon tamoxifen administration were confirmed in peritoneal macrophages isolated from AOM/DSS-treated $Egfr^{\Delta MyI\text{-}ER}$ mice (Fig. S1A, B, and Suppl. Mat. 1A). 40-50 days after tamoxifen administration and EGFR deletion, colorectal tumor areas were significantly reduced in $Egfr^{\Delta MyI\text{-}ER}$ mice, while the number of tumors remained the same (Fig. 1B, C). Interestingly, in $Egfr^{\Delta MyI}$ mice, tumor numbers were reduced compared to controls, suggesting that EGFR expression in myeloid cells enhances tumor initiation in the early phases (Fig. 1C). Therefore, EGFR signaling in myeloid cells regulates the initiation and promotion of colon tumors in the AOM/DSS tumor model, highlighting its therapeutic relevance.

To determine the myeloid cell populations in which EGFR is deleted, we assessed the recombination efficiency in AOM/DSS tumors of *LysM-Cre* x *LSL-YFP* reporter mice [16]. YFP expression, and thus recombination, was highest in granulocytes, followed by macrophages, monocytes, and dendritic cells (DCs) (Fig. S1C, D). Reduced *Egfr* expression was confirmed in granulocytes and macrophages sorted from AOM/DSS tumors (Fig. S1E). Moreover, we were able to detect reduced EGFR protein levels in cultured peritoneal macrophages of $Egfr^{\Delta MyI}$ AOM/DSS-treated mice (Fig. S1F and Suppl. Mat. 1B). These results indicate that *Egfr* is effectively deleted in various myeloid populations, including granulocytes and macrophages of $Egfr^{\Delta MyI}$ tumors.

To exclude that EGFR deletion in DCs is responsible for reduced tumor growth, we crossed $Egfr^{fl/fl}$ to *CD11c-Cre* mice ($Egfr^{\Delta Cd11c}$) and analyzed the AOM/DSS-induced tumor burden. Recombination of *Egfr* was confirmed in splenic DCs, along with the absence of *Egfr* expression (Fig. S1G, and Suppl. Mat. 1C). However, no difference in tumor area or number could be detected (Fig. 1D, E) excluding that EGFR deletion in DCs is responsible for reduced CRC development.

We next investigated whether EGFR deletion affects the myeloid infiltrates in AOM/DSS tumors. Flow cytometry of $Egfr^{\Delta MyI}$ tumors showed that the numbers of F4/80^{hi} macrophages and monocytes were reduced, while no quantitative differences were observed in granulocytes, F4/80^{lo} myeloid cells, or conventional DC1 (cDC1) populations (Fig. 1F). Reduced macrophage infiltration was further confirmed following myeloid-specific EGFR deletion in already established tumors using the inducible $Egfr^{\Delta MyI\text{-}ER}$ model, as determined by multiplex immunofluorescence on AOM/DSS tumor sections (Fig. 1G, H). Therefore, we conclude that EGFR deletion in myeloid cells reduces the number of macrophages and monocytes in the TME of CRC.

Single-cell transcriptomics reveals an altered colorectal TME upon EGFR deletion in myeloid cells

To elucidate how EGFR expression in myeloid cells affects the global CRC TME, we sorted CD45-negative (CD45$^-$) and CD45-positive (CD45$^+$) cells from AOM/DSS-induced colorectal tumors pooled from three $Egfr^{fl/fl}$ and three $Egfr^{\Delta MyI}$ mice and performed 10x scRNAseq (Fig. S2A). After quality control and filtering, we obtained 8,284 cells from $Egfr^{fl/fl}$ tumors and 4,758 cells from $Egfr^{\Delta MyI}$ tumors (Fig. S2B). To define the major populations of these tumors, we combined the four resulting datasets, performed graph-based clustering, and annotated each cluster based on canonical marker gene expression (Fig. S2C–E and Table S1). To ensure that unsupervised clustering captured intrinsic cell identity and transcriptional state rather than differences in proliferation, cell cycle regression was applied prior to dimensionality reduction and clustering. This step minimized gene expression variation attributable to cell cycle phase. After cell cycle regression, cells were classified into 22 clusters (Fig. 2A). We detected a high number of myeloid cells, including neutrophils expressing *Csf3r* (Cluster 0, 13), monocytic and macrophage populations marked by *Fcgr1* (Cluster 1, 3), as well as DCs defined by *Flt3* expression

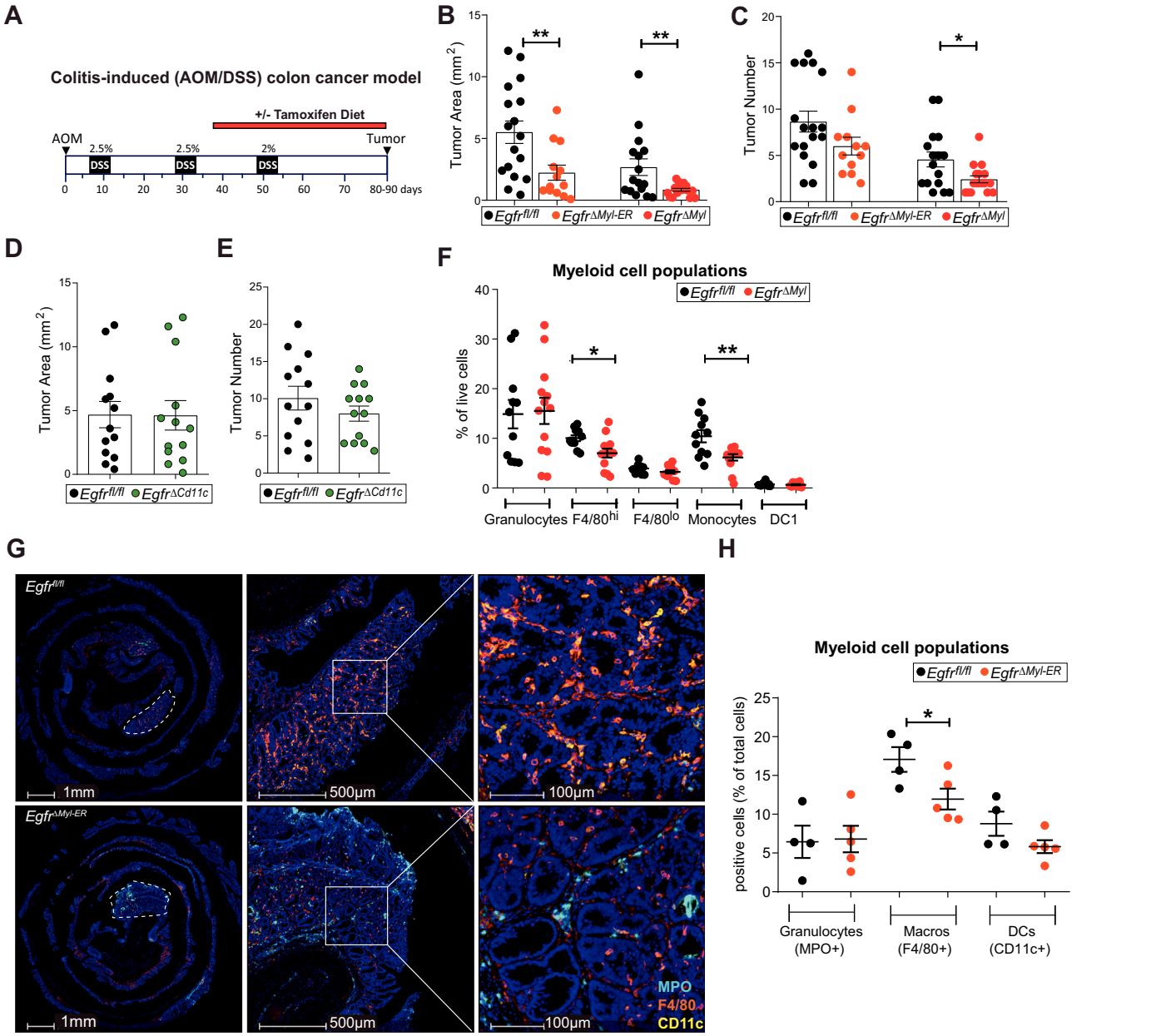


Fig. 1 EGFR deletion in myeloid cells reduces tumor burden of colitis-associated intestinal tumorigenesis. A Overview of AOM/DSS model used to induce colitis-associated colorectal tumors. *LysM-CreER*^{T2} activation was induced by a tamoxifen diet when tumors had developed and continued for 40–50 days. Tamoxifen was also fed to control *Egfr*$^{fl/fl}$ mice. Analysis of tumor burden in respective AOM/DSS-treated mice: **B** Tumor area and **C** tumor number after *Egfr* deletion in myeloid cells of established tumors in *Egfr*$^{\Delta Myl\text{-}ER}$ mice ($n = 13$ and $n = 12$) compared to respective *Egfr*$^{fl/fl}$ control ($n = 17$), *Egfr*$^{\Delta Myl}$ mice ($n = 16$), constitutively lacking *Egfr* in myeloid cells, and their controls (*Egfr*$^{fl/fl}$, $n = 16$). **D** Tumor area and **E** tumor number in mice lacking *Egfr* in dendritic cells (*Egfr*$^{\Delta Cd11c}$, $n = 13$) and controls (*Egfr*$^{fl/fl}$, $n = 13$). **F** Quantification of granulocytes, F4/80^{hi} macrophages, F4/80^{lo} myeloid cells, monocytes, and DC1s among live cells in *Egfr*$^{\Delta Myl}$ ($n = 13$) and *Egfr*$^{fl/fl}$ ($n = 11$) AOM/DSS tumors using flow cytometry. **G** Representative multiplex immunofluorescence staining of *Egfr*$^{fl/fl}$ *and Egfr*$^{\Delta Myl\text{-}ER}$ tumors. Staining panel included antibodies against MPO, F4/80, and CD11c. DAPI was used for nuclei detection. Circles and lines indicate which area is shown magnified. Magnification: x1, x5, x20. Scale bars: 1 mm, 500 µm, 100 µm. **H** Quantification of the MPO-, F4/80-, and CD11c-positive cells within AOM/DSS tumors (*Egfr*$^{fl/fl}$, $n = 4$; *Egfr*$^{\Delta Myl\text{-}ER}$, $n = 5$). All data are plotted as mean ± SEM with each data point representing a mouse. **B–F** Data from three independent experiments are shown. Statistical analysis was performed by unpaired Student's t test $^{*}P < 0.05$, $^{**}P < 0.01$.

(Cluster 8, 12, 17), and a small cluster of mast cells expressing *Mcpt* (Cluster 16). F4/80^{hi} (*Adgre1*^{hi}) macrophages were defined by *C1qc* expression (Cluster 1), whereas high *Spp1* and *Vegfa* expression characterized a mixed population of macrophages and monocytes (Cluster 3) [17]. Lymphocytes were identified as B cells by *Cd79a* (Cluster 2, 19), plasma cells expressing *Jchain* (Cluster 10), and T cells positive for *Tcrb* and *Cd3e* (Cluster 5, 6, 7, 11, 18). Among CD45^{-} cells, we detected *Epcam*$^{+}$ epithelial cells (Cluster 4, 14, 15), *Col3a1*$^{+}$ fibroblasts (Cluster 20), and a mixed proliferating cluster expressing high *Mki67* and *Top2a* (Cluster 9) (Figs. 2A and S2D, E).

EGFR deletion in myeloid cells resulted in quantitative alterations in populations within the TME of AOM/DSS-tumors (Fig. 2A, B). *Egfr*$^{\Delta Myl}$ tumors displayed reduced numbers of granulocytes and macrophages compared to *Egfr*$^{fl/fl}$. In contrast, numbers of T and B cells were increased, indicating an additional effect on the lymphoid compartment of those tumors (Fig. 2B and Table S2).

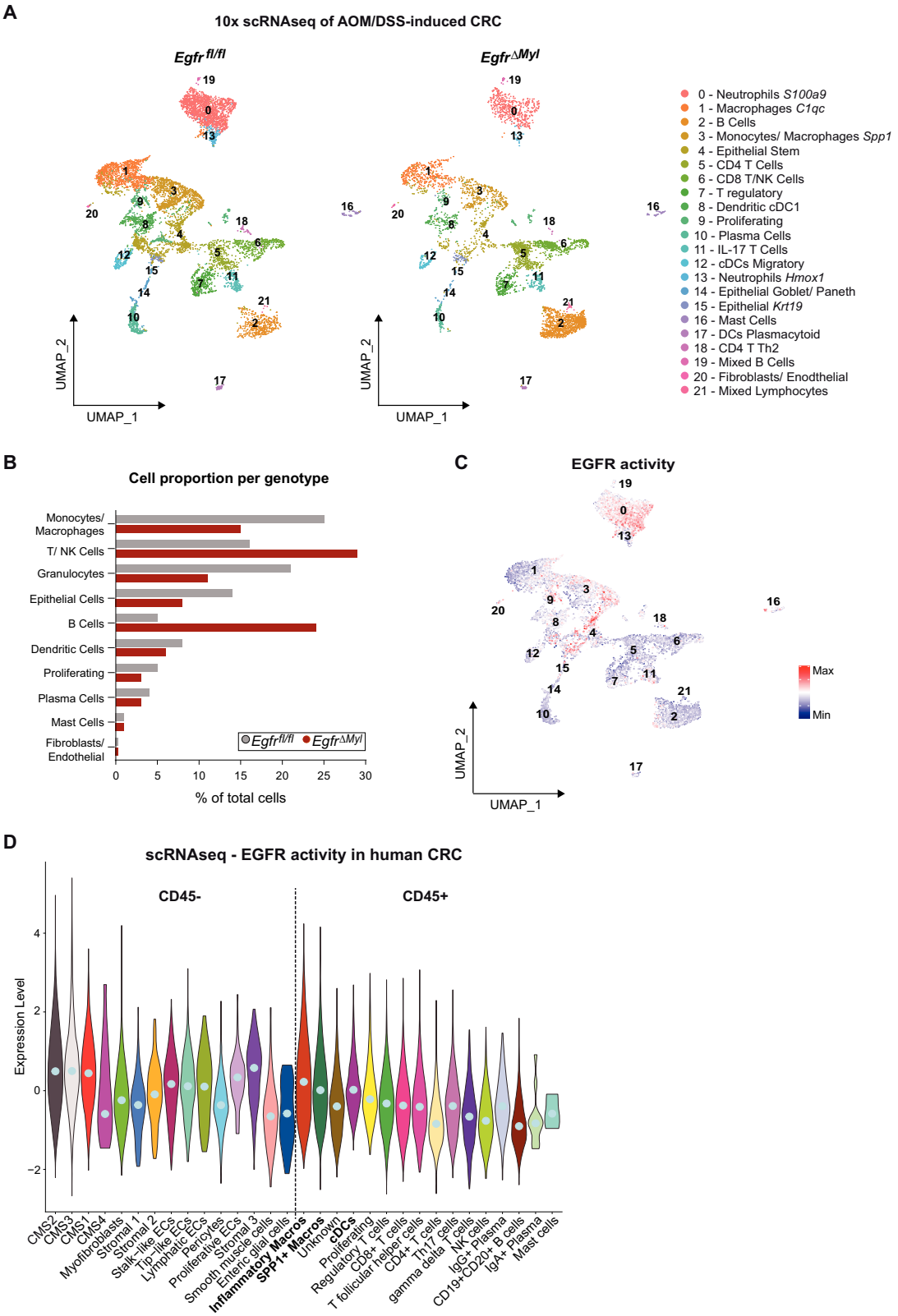


Fig. 2 Single-cell transcriptomics reveals an altered colorectal tumor microenvironment upon EGFR deletion in myeloid cells. A UMAP plots of immune and non-immune cells ($n = 13{,}042$ cells in total) from sorted colon tumors of AOM/DSS-treated *Egfr*$^{fl/fl}$ ($n = 3$) and *Egfr*$^{\Delta Myl}$ ($n = 3$) mice, showing 22 cell clusters (10x scRNAseq). Each cluster is represented by a different color. **B** Bar graph showing relative distribution (%) of major cell types in *Egfr*$^{fl/fl}$ (gray) and *Egfr*$^{\Delta Myl}$ (red) AOM/DSS tumors. **C** UMAP of EGFR pathway activity scores analyzed by PROGENy among different clusters of AOM/DSS colon tumors in a combined background. Red indicates high expression and blue low expression. **D** Violin plots depicting EGFR pathway activity across different cell populations in human colorectal tumors (10x scRNAseq) assessed by PROGENy.

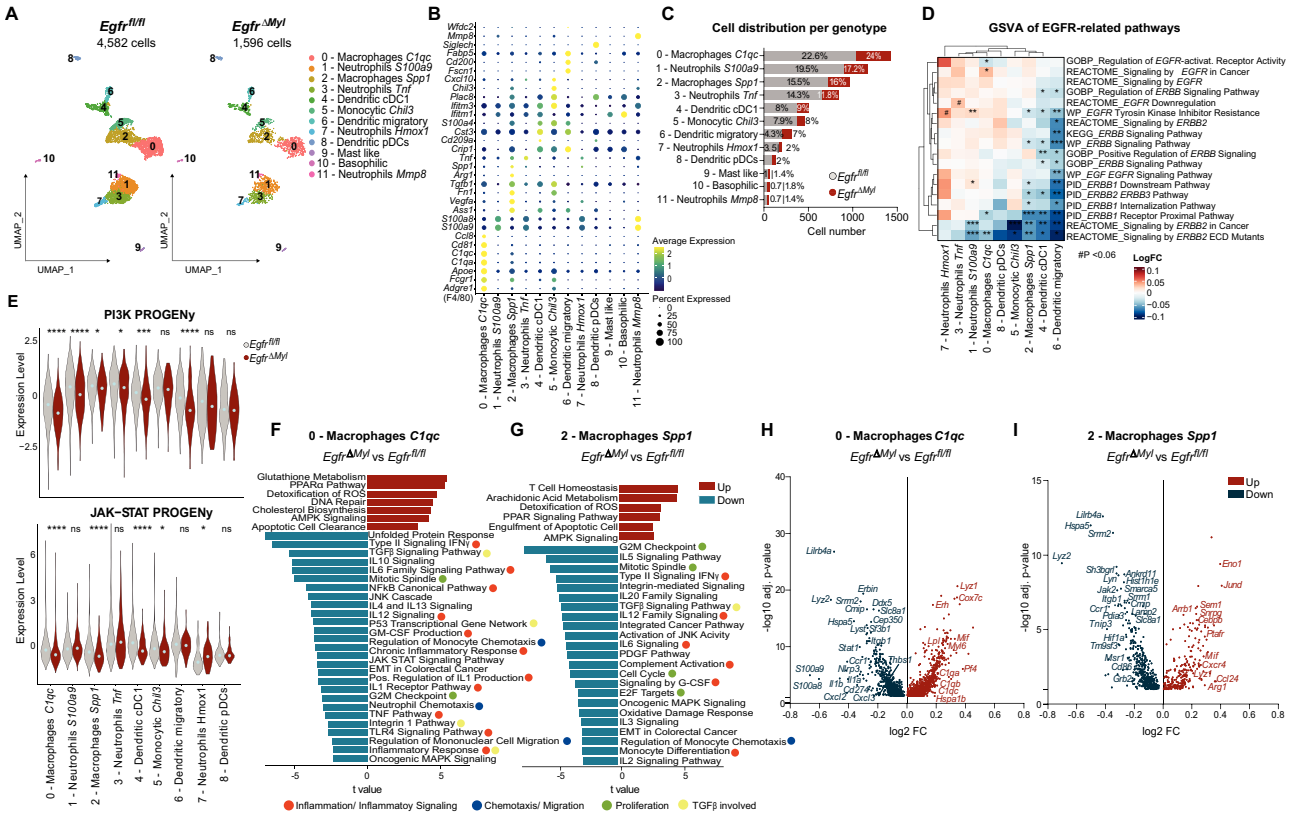


Fig. 3 **Lack of EGFR in myeloid cells impairs signaling in myeloid cells. A** UMAP of the myeloid cell composition, colored by clusters, in *Egfr*$^{fl/fl}$ and *Egfr*$^{\Delta Myl}$ tumors (10x scRNAseq). **B** Dot plot of top-differentially expressed genes per cluster. Color intensity reflects the strength of expression, and dot size indicates the percentage of cells expressing the genes in each cluster. **C** Bar graph showing relative distribution (%) of myeloid subsets among *Egfr*$^{fl/fl}$ (gray) and *Egfr*$^{\Delta Myl}$ (red) AOM/DSS tumors. **D** Heatmap of differentially enriched EGFR-related pathways and biological processes in *Egfr*$^{\Delta Myl}$ vs *Egfr*$^{fl/fl}$ myeloid clusters, analyzed by GSVA. Significance was assessed using empirical Bayesian moderated t-statistics adjusted with Benjamini-Hochberg. **Padj* < 0.05, ***Padj* < 0.01, ****Padj* < 0.001. **E** PROGENy analyses of EGFR downstream signaling pathways PI3K and JAK/STAT. Wilcoxon rank-sum test **P* < 0.05, ****P* < 0.001, *****P* < 0.0001. Differential pathways and biological processes enriched in *Egfr*$^{\Delta Myl}$ and *Egfr*$^{fl/fl}$ **F** macrophages *C1qc* and **G** macrophages *Spp1* by GSVA (*Padj* < 0.05). **H, I** Differentially expressed genes in *Egfr*$^{\Delta Myl}$ vs *Egfr*$^{fl/fl}$. **H** macrophages *C1qc* and **I** macrophages *Spp1*, using limma with Benjamini–Hochbergadjusted P values (*Padj* < 0.05).

Egfr mRNA was detected only in a few cells, mainly in epithelial cells and fibroblasts, where expression is known to be high (data not shown). This is not surprising since the average coverage for individual genes from scRNAseq using the 10x platform can be low [17]. Therefore, to assess EGFR activity in cell populations of colorectal tumors, we analyzed single-cell data from AOM/DSS tumors and human CRC using PROGENy, an algorithm that estimates the activity of relevant signaling pathways based on consensus gene signatures obtained from perturbation experiments [18]. Besides epithelial cells, EGFR activity was the highest in neutrophils expressing high levels of *S100a9*, as well as in the *Spp1*$^{+}$ macrophage/monocyte cluster of AOM/DSS tumors (Fig. 2C). Next, we checked the relevance of our findings in the human CRC TME by analyzing a published CRC cohort profiled using the same technology [19]. In line with our murine observations, clusters of inflammatory and *SPP1*$^{+}$ macrophages displayed the highest EGFR activity scores (among all immune subsets), also in the re-analyzed human CRC data (Fig. 2D). Taken together, our data indicate that EGFR deletion in myeloid cells leads to a shift in the immune infiltrate of AOM/DSS tumors characterized by reduced numbers of granulocytes and macrophages and an increased number of T cells. In addition, EGFR activity appears to be the highest in *Spp1*$^{+}$ macrophages in both mouse and human CRC, suggesting a specific role of EGFR signaling in this subpopulation of macrophages.

Impaired signaling in myeloid cells lacking EGFR

To investigate the impact of EGFR expression on myeloid cell signaling and its related tumor-promoting role, we subclustered the myeloid cell populations to increase the subset specificity and characterize differential RNA expression patterns in depth. The classification of the myeloid-specific clusters was based on previous publications [17, 20]. We identified two major macrophage clusters, a *C1qc* cluster marked by high expression of *Adgre1* (F4/80, Cluster 0) and one expressing *Spp1* and *Vegfa* (Cluster 2) (Fig. 3A, B and Table S3). Both types of macrophages have previously been described to support tumor growth [11, 12, 19, 21]. Neutrophils subclustered into four subsets characterized by the inflammatory genes *S100a8* and *S100a9*, *Tnf*, *Hmox1*, and *Mmp8*, respectively (Cluster 1, 3, 7, 11). Furthermore, we identified *Chil3* monocytes (Cluster 5) and three clusters of DCs, cDC1 marked by *Cst3* expression, migratory myeloid regulatory DC3 cells characterized by *CD200* as well as *Fscn1* expression [22, 23], and plasmacytoid DCs (pDCs) expressing *Siglech* [24] (Cluster 4, 6, 8). Most *Zbtb46* and *Sirpa*-expressing cDC2 cells clustered with migratory DCs (data not shown). AOM/DSS tumors also contained very low numbers of mast and basophil-like cells (Cluster 9, 10) (Figs. 3A, B and S2D, E). Although the overall number of myeloid cells was reduced in *Egfr*$^{\Delta Myl}$ tumors, we did not observe differences in relative percentages between the corresponding clusters (Figs. 2B and 3C and Table S2).

Since we could not directly detect *Egfr* mRNA in myeloid cells, we performed Gene Set Variation Analysis (GSVA) on $Egfr^{\Delta Myl}$ *vs* $Egfr^{fl/fl}$ cell clusters to quantify differences in EGFR-related signaling pathways (Fig. 3D). Interestingly, these were most downregulated in both cDC clusters, followed by $Spp1^{+}$ and $C1qc^{+}$ macrophages. This was unexpected since our data demonstrated that the highest *LysM-Cre*-mediated *Egfr* recombination occurs in granulocytes (Fig. S1D). In contrast, neutrophilic granulocytes, especially those expressing *Hmox1*, showed an upregulation of EGFR-associated pathways, potentially due to activated compensatory mechanisms (Fig. 3D).

Signaling pathways downstream of EGFR include ERK/MAPK, PI3K/AKT, and JAK/STAT. To investigate which of these pathways may be perturbed among EGFR-deficient myeloid cells, we used PROGENy (Table S4). The results confirmed altered EGFR signaling in *S100a9* neutrophils and migratory DCs (Fig. S3A). However, the PI3K signature was decreased in all macrophage, neutrophil, and DC subsets, excluding monocytes, *Hmox*1 neutrophils, and pDCs (Fig. 3E). Moreover, JAK/STAT activity was reduced in macrophages, monocytes, and cDC1s of $Egfr^{\Delta Myl}$ tumors, whereas it was increased or unchanged in granulocytes (Fig. 3E).

Additionally, GSVA revealed strong downregulation of inflammation-related pathways such as interferon γ (IFNγ), IL6, IL12, and transforming growth factor β (TGFβ*)* signaling in both macrophage clusters. IFNγ and IL6 pathways were also attenuated in monocytes. $C1qc^{+}$ macrophages additionally showed downregulation of the IL1 pathway. Importantly, migration and proliferation-related pathways such as the mitotic spindle and G2M checkpoint were downregulated in both macrophage clusters, possibly contributing to the reduced numbers we observed in $Egfr^{\Delta Myl}$ tumors. In contrast, pathways related to lipid anabolism, PPARα, ROS and glutathione metabolism were upregulated in $Egfr^{\Delta Myl}$ macrophages, suggestive of high metabolic activity in $C1qc^{+}$ and $Spp1^{+}$ macrophages (Figs. 3F, G and S3B). Interestingly, *Chil3*-expressing monocytes showed increased expression of genes regulating phagocytic activity and genes interfering with epithelial cell migration, possibly counteracting the invasive potential of CRC cells (Fig. S3B). Thus, we conclude that EGFR deletion leads to distinct effects on specific myeloid cell subpopulations in AOM/DSS tumors by altering the activity of signaling pathways involved in inflammation, proliferation, migration, and survival.

C1qc macrophages of $Egfr^{\Delta Myl}$ tumors additionally showed a significant reduction of genes encoding the inflammatory cytokines *Il1a* and *Il1b*, chemokines *Cxcl2* and *Cxcl3*, calcium-binding proteins *S100a8* and *S100a9*, and *Thbs1*, encoding thrombospondin-1. Importantly, genes that have been linked to suppressive phenotypes in myeloid cells, such as *Cd274* (encoding PDL1), were also downregulated (Fig. 3H). $Spp1^{+}$ macrophages demonstrated a reduction of the co-stimulatory gene *Cd86* and the scavenger receptor *Msr1* gene (Fig. 3I). Interestingly, in monocytes as well as $C1qc^{+}$ and $Spp1^{+}$ macrophages, the expression of the chemokine receptor *Ccr1*, known to be involved in cell recruitment, was reduced (Figs. 3H, I and S3C). In both macrophage populations, we observed reduced expression of the checkpoint gene *Lilrb4a*, and reduction of genes of the JAK/STAT pathway, such as *Stat1* in $C1qc^{+}$ and *Jak2*, and *Tnaip3* in $Spp1^{+}$ macrophages (Fig. 3H, I and Table S5). Similarly, monocytes showed a downregulation of IFN-activated genes (Fig. S3C). In contrast, the gene encoding the inflammatory cytokine *Mif* was expressed at higher levels in $C1qc^{+}$ and $Spp1^{+}$ macrophages, whereas *Cxcr4* was upregulated in $Spp1^{+}$ macrophages and monocytes (Figs. 3H, I and S3C). MIF and CXCR4 may form complexes promoting leukocyte recruitment [25].

Taken together, our data show that *Egfr* deletion in myeloid cells leads to the downregulation of PI3K and JAK/STAT signaling and to an impairment of key processes linked to inflammation, migration, and proliferation in $C1qc^{+}$ and $Spp1^{+}$ TAMs. Since EGFR activity is stronger in $Spp1^{+}$ macrophages (Fig. 2C), this indicates that the lack of EGFR in $Spp1^{+}$ macrophages might cause cell-autonomous effects, whereas the altered gene expression we observe in $C1qc^{+}$ macrophages is potentially also mediated through cell-extrinsic factors.

EGFR deletion in myeloid cells reduces immunosuppression in CRC

Among the most prominent differences we observed between $Egfr^{fl/fl}$ and $Egfr^{\Delta Myl}$ tumors was a change in the abundance of T cell subpopulations (Fig. 2A, B). T cell infiltration into tumor tissue and their phenotype therein are important prognostic parameters for the outcome and therapy response of human CRC [15, 26]. Thus, we characterized the differences within the T cell compartment of $Egfr^{\Delta Myl}$ tumors. To achieve a more rigorous separation, we employed a selective subclustering approach focusing on genes expressed by different T lymphocyte populations [27, 28]. Using this strategy, we were able to identify 9 different subclusters (Figs. 4A, B and S4A; Table S6): CD4 T cell populations (Cluster 0, 1, 2, 4), three CD8 T cell populations (Cluster 3, 5, 6) and two clusters containing innate lymphocytes (Cluster 7, 8).

T_{regs} represented the most prominent cluster among T cells and showed high *Foxp3* and *Ctla4* expression levels, and their number was significantly reduced in mice lacking EGFR in myeloid cells (Fig. 4C). Memory cells (Cluster 2) expressing *Tnfsf8* and *Cd40lg* were also reduced in $Egfr^{\Delta Myl}$ tumors, while naïve-like cells (Cluster 1, 3) marked by *Lef1* and *Sell* were increased (Fig. 4C). Importantly, CD8 exhausted cells (Cluster 6) expressing *Klrd1* and *Pdcd1* were detected with a lower frequency in $Egfr^{\Delta Myl}$ tumors, indicative of an immunostimulatory environment (Fig. 4C). Flow cytometry analysis of independent AOM/DSS tumors allowed us to confirm the reduction of T_{regs} among CD4 T cells in $Egfr^{\Delta Myl}$ tumors. In contrast, relative numbers of naïve or memory-like T cells were unchanged (Figs. 4D and S4B, C).

Differential gene expression analysis of CD4 and CD8 T cells in $Egfr^{\Delta Myl}$ tumors revealed a reduction in exhaustion-related markers such as *Ctla4*, *Pdcd1, and Lilrb4* in CD4 as well as CD8 T cells (Fig. 4E, F and Table S7). CD8 T cells further showed reduced expression of immune checkpoint genes *Havcr2* and *Gzmk* (Fig. 4F). Additionally, *Ifngr1* and *Ccl5* were downregulated in both T cell populations, while markers associated with a naïve-like or tissue-resident T cell phenotype, such as *Sell*, *Tcf7*, and *Lef1*, were upregulated (Fig. 4E, F). Differentially expressed genes in T_{regs} included *Pcsk1*, *Areg*, and *Lilrb4*, which have been described in activated T_{regs} (Fig. 4G).

In conclusion, our data indicate that EGFR deletion in myeloid cells leads to a shift in the phenotype of T cells infiltrating AOM/DSS tumors towards a less suppressive milieu, mirrored by a reduction in T_{reg} cell numbers and less exhausted CD8 T cells.

Predicted cell-cell communication networks are altered between myeloid cells and T cells in CRC of $Egfr^{\Delta Myl}$ mice

Having observed altered chemokine and cytokine signaling in EGFR-deficient myeloid cells, we next aimed at further mining the generated scRNAseq dataset to infer how cells communicate in the colorectal TME. Therefore, we applied CellChat to computationally predict candidate intercellular communication networks [29]. Initially, we specified the most prominent predicted interactions and pathways within AOM/DSS tumors, based on the highest calculated probabilities. High-ranked pathways included co-stimulatory molecules (PDL1, CD80, CD86), chemokines, and cell-interaction pathways (NECTIN, CD226), which were downregulated in $Egfr^{\Delta Myl}$ tumors. In contrast, MHC-I, CD23, and ICOS-related pathways were enriched in $Egfr^{\Delta Myl}$ tumors (Fig. S5A). Moreover, signals originating from myeloid cells were predominantly directed towards T cells and were the most abundant within $Egfr^{fl/fl}$ tumors (Fig. 5A). Ligand-receptor pairs, such as

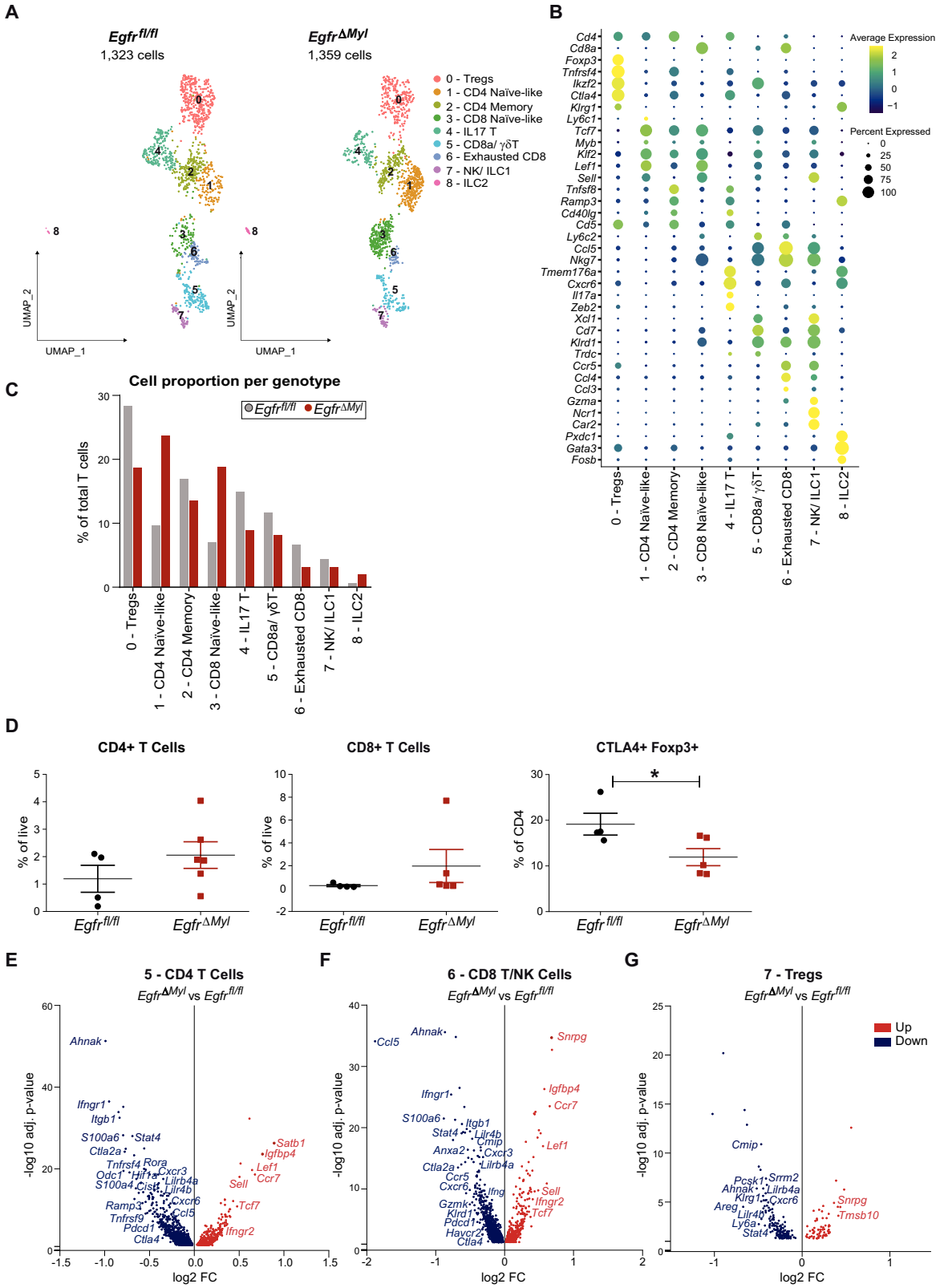
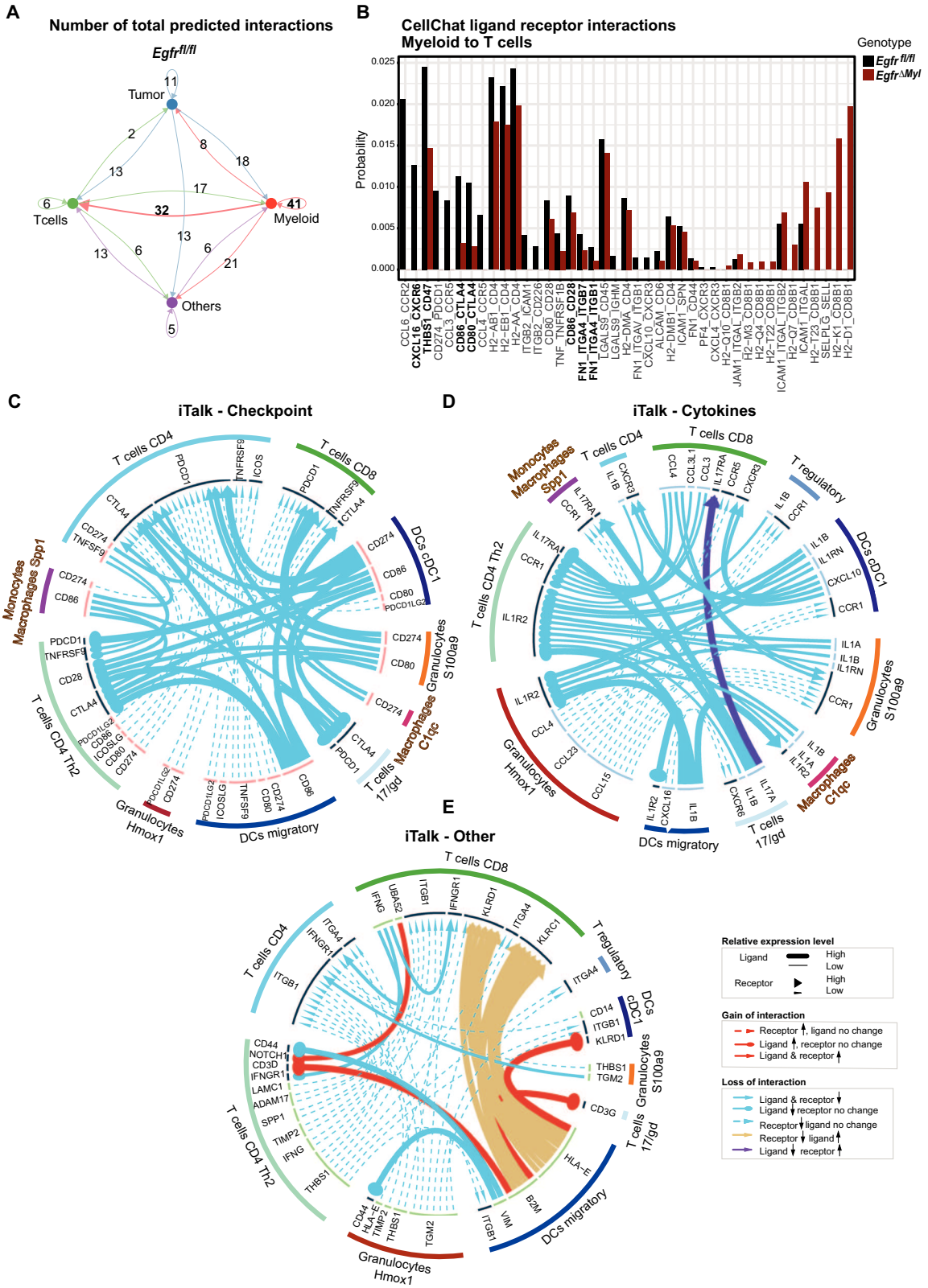


Fig. 4 EGFR deletion in myeloid cells reduces immunosuppression in CRC. A UMAP showing the composition of T/NK/ILC cells in 10x scRNAseq of *Egfr*$^{fl/fl}$ and *Egfr*$^{\Delta Myl}$ AOM/DSS tumors, colored by clusters. **B** Dot plot of top-differentially expressed genes in respective clusters. Color intensity represents expression level, and dot size indicates the percentage of cells expressing the genes within each cluster. **C** Relative distribution (%) of T/NK/ILC subclusters in *Egfr*$^{fl/fl}$ (gray) and *Egfr*$^{\Delta Myl}$ (red) AOM/DSS tumors. **D** Quantification of CD4$^+$ and CD8$^+$ T cells among live cells, and Foxp3$^+$ CTLA4$^+$ among CD4$^+$ cells in AOM/DSS tumors (*Egfr*$^{fl/fl}$, $n = 4$; *Egfr*$^{\Delta Myl}$, $n = 5$) using flow cytometry, unpaired Student's t test $^*P < 0.05$. Data are plotted as mean ± SEM with each data point representing a mouse. Volcano plots showing differential gene expression of total **E** CD4 and **F** CD8 T cells and **G** T_{regs} in *Egfr*$^{\Delta Myl}$ vs *Egfr*$^{fl/fl}$ tumors using limma with Benjamini–Hochberg-adjusted P values (*Padj* < 0.05).



THBS1-CD47, H2AA/AB1-CD4, CCL6-CCR2, and CD80/86-CTLA4, displayed the highest probability scores in *Egfr*$^{fl/fl}$ tumors (Figs. 5B and S5B). The predicted changes in interactions upon *Egfr* deletion in myeloid cells suggested an altered cross-talk with T cells, as reflected by differences in the probabilities of several ligand-receptor pairs. Specifically, interactions including CCL6-CCR2, CXCL16-CXCR6, THBS1-CD47, CD274-PDCD1, and CD80/86-CTLA4 displayed a reduced probability, whereas the probability for H2-K1/D1-CD8B1 T cell interaction was increased in *Egfr*$^{\Delta Myl}$ tumors (Fig. 5B).

Fig. 5 Altered cell interactions among myeloid and T cells in *Egfr*$^{\Delta Myl}$ mouse CRC tumors. A Predicted ligand-receptor interactions among tumor, myeloid, T, and other cell clusters in *Egfr*$^{fl/fl}$ tumors calculated by CellChat. **B** Top 212 interaction probabilities were calculated by CellChat, and each probability displayed was significant (*Padj* < 0.05). Myeloid-to-T cell interaction scores are displayed in descending probability difference of *Egfr*$^{fl/fl}$ to *Egfr*$^{\Delta Myl}$. Ligand-receptor pairs in bold are in line with iTalk results (Suppl. Fig. 5C). **C**–**E** iTalk-based analysis of predicted gain (red) and/or loss (blue, brown, or purple) of ligand-receptor interactions among myeloid and T cell clusters in *Egfr*$^{\Delta Myl}$ vs *Egfr*$^{fl/fl}$ tumors. Solid lines mark significant changes for the ligand, and dashed lines indicate no significant changes for the ligand. An arrow marks significant changes for the receptor, and an ellipse indicates no significant change for the receptor. Line and scheme width indicate relative expression levels. Strength scores represent the product of ligand and receptor fold changes; the top 50 interaction scores are displayed (*Padj* < 0.05). Circos plots show the top 50 predicted ligand-receptor interactions for **C** Checkpoint, **D** Cytokines, and **E** Other. The explanatory scheme in **E** is adapted from Wang et al., 2019.

To further characterize myeloid-T cell interactions in *Egfr*$^{fl/fl}$ and *Egfr*$^{\Delta Myl}$ tumors, we applied an orthogonal, computational approach, iTalk [30]. Similar to CellChat, iTalk identified altered ligand–receptor interactions related to checkpoint and cytokine regulation (Fig. S5C). Remarkably, a decrease in CD274-PDCD1 interaction was predicted, in line with the downregulation of the CD274 ligand in *C1qc*$^{+}$ macrophages, cDC1 and *S100a9* granulocytes, as well as with reduced expression of the PDCD1 receptor in T cells (Fig. 5C and Table S8). Importantly, CD86-CTLA4 interaction was also reduced due to decreased availability of the ligand CD86 in *Spp1*$^{+}$ monocytes/macrophages and DCs, and CTLA4 originating from T cells. In addition, interactions of CD4 T cells through ICOS were also found downregulated. Cytokine-related networks were also affected, with predicted loss of IL1A/B-IL1R2/IL1RN ligand-receptor pairs between different myeloid and T cell clusters. Specifically, IL1-related signals originating from granulocytes, macrophages, and DCs directed towards CD4 T cells were significantly downregulated (Fig. 5D). Other interactions that were downregulated within the *Egfr*$^{\Delta Myl}$ TME included the THBS1-ITGB1/ITGA4 *pairs*, with significantly lower THBS1 ligand probability from myeloid to T cell subsets (Fig. 5E and Table S8). Significant loss of a THBS1-CD47 interaction between THBS1-expressing *C1qc*$^{+}$ macrophages and CD47-expressing CD4, CD8, and regulatory T cells was also computationally identified (*Padj* value = 0.01; Table S8).

Taken together, our data suggest a possible decrease in the cross-talk between myeloid and T cells in AOM/DSS tumors of Egfr$^{\Delta Myl}$ mice, involving immune checkpoint and cytokine ligand-receptor pairs.

Integration of proteomic data with single-cell transcriptomics of myeloid cells reveals common targets in macrophages

We next sought to investigate whether the changes observed at the RNA level translate into altered protein expression. Since the number of sorted myeloid cells retrieved from murine AOM/DSS tumors is not sufficient for immunoblot analyses, we sorted granulocytes, macrophages, and monocytic populations from *Egfr*$^{fl/fl}$ and *Egfr*$^{\Delta Myl}$ tumors and performed nano-flow mass spectrometry.

After quantification and normalization, we were able to identify an average of 4000–5000 distinct proteins per sample (Fig. S6A). A comparison of the two biological replicates within each cell population revealed only small variations (Fig. S6B). Differential protein expression analysis unveiled alterations across all different cell populations between the two genotypes (Fig. S6C). F4/80^{+} macrophages of *Egfr*$^{\Delta Myl}$ tumors exhibited a reduction of thrombospondin proteins THBS1 and THBS4, as well as of members of insulin signaling and the coagulation machinery [31]. In addition, we observed an upregulation of proteins involved in antigen uptake and processing, such as LAMP2, ITGAM, and PSME1 (Fig. 6A and Table S9). We compared genes differentially expressed by scRNAseq to corresponding proteins in *Egfr*$^{\Delta Myl}$ *vs* *Egfr*$^{fl/fl}$ tumors. Among the different sorted myeloid populations, macrophages showed most of the common targets (Figs. 6B and S6D; Table S9).

Importantly, *Thbs1* and *Plek* were downregulated on both RNA and protein levels in *Egfr*$^{\Delta Myl}$ tumors (Fig. 6B). Both proteins have been shown to be important in activated macrophages [32, 33]. In line with this finding, we were further able to detect co-expression of EGFR and THBS1 in tumor-associated macrophages, confirming the presence of these cells in the TME of murine CRC (Fig. 6C).

Interestingly, the relative difference between *Egfr*$^{\Delta Myl}$ and *Egfr*$^{fl/fl}$ samples was more pronounced at the protein than at the RNA level, suggesting additional post-transcriptional mechanisms that control the expression patterns of those proteins. Mutually upregulated molecules included *Mif*, which has been associated with colitis and tumor-associated macrophages [25], and *Bax*, which has been linked to the induction of apoptosis, possibly explaining the reduced macrophage numbers in *Egfr*$^{\Delta Myl}$ tumors (Figs. 6B and 1F) [34]. In contrast, granulocytes and monocytes demonstrated limited correlation between RNA and protein expression, suggesting that these populations exhibit high plasticity and rapid shifts within the TME (Fig. S6D). Based on our findings, we conclude that EGFR signaling in myeloid populations influences both their transcriptome and proteome in AOM/DSS tumors. In addition, a comparison of transcriptional and translational changes indicates that macrophages are affected by *Egfr* deletion, highlighting THBS1 as a potential target that influences surrounding cell populations.

The EGFR pathway is active in inflammatory and *SPP1*$^{+}$ myeloid cells in human CRC

Having defined the role of EGFR in distinct myeloid cell populations and its influence on their interactions with T cells within the TME, we next sought to determine the relevance of our findings in human CRC. Using the human CRC scRNAseq dataset described by *Lee et al.* [19], we first applied PROGENy to assess EGFR pathway activity in the different cell populations. Among the myeloid populations, we detected high activity within inflammatory and *SPP1*$^{+}$ macrophage clusters (Figs. 2D and 7A). We then stratified the cells within the human macrophage clusters based on high or low *EGFR* pathway activity (*EGFR*^{high} or *EGFR*^{low}). To validate differentially expressed genes from our *Egfr*$^{\Delta Myl}$ *vs* *Egfr*$^{fl/fl}$ murine macrophage clusters, we compared them to differentially expressed genes in *EGFR*^{low} *vs* *EGFR*^{high} human macrophages. In line with the results obtained from murine macrophages of AOM/DSS tumors, genes including *IL1A*, *IL1B*, *IL6*, *CXCL2*, *THBS1*, and *S100A8/9* were downregulated in *EGFR*^{low} inflammatory macrophages (Fig. 7B and Table S10). Human *SPP1*$^{+}$ macrophages with *EGFR*^{low} activity also showed downregulation of the orthologous genes identified in the mouse data, including *IL1A*, *IL1B, CXCL2, and PLEK* (Fig. 7C and Table S10). Interestingly, genes encoding ligands of *EGFR*, such as *AREG* and *EREG*, were also significantly downregulated in both *EGFR*^{low} macrophage clusters, indicating possible autocrine and paracrine loops connected to *EGFR* signaling in these cells (Fig. 7B, C). These findings demonstrate extensive similarity between genes affected in the myeloid cells of mouse and human CRC.

Leveraging available scRNAseq data from human CRC cohorts of very limited size to predict survival outcomes represents a major challenge. To overcome this limitation, we analyzed a publicly available dataset of 516 patients, consisting mostly of

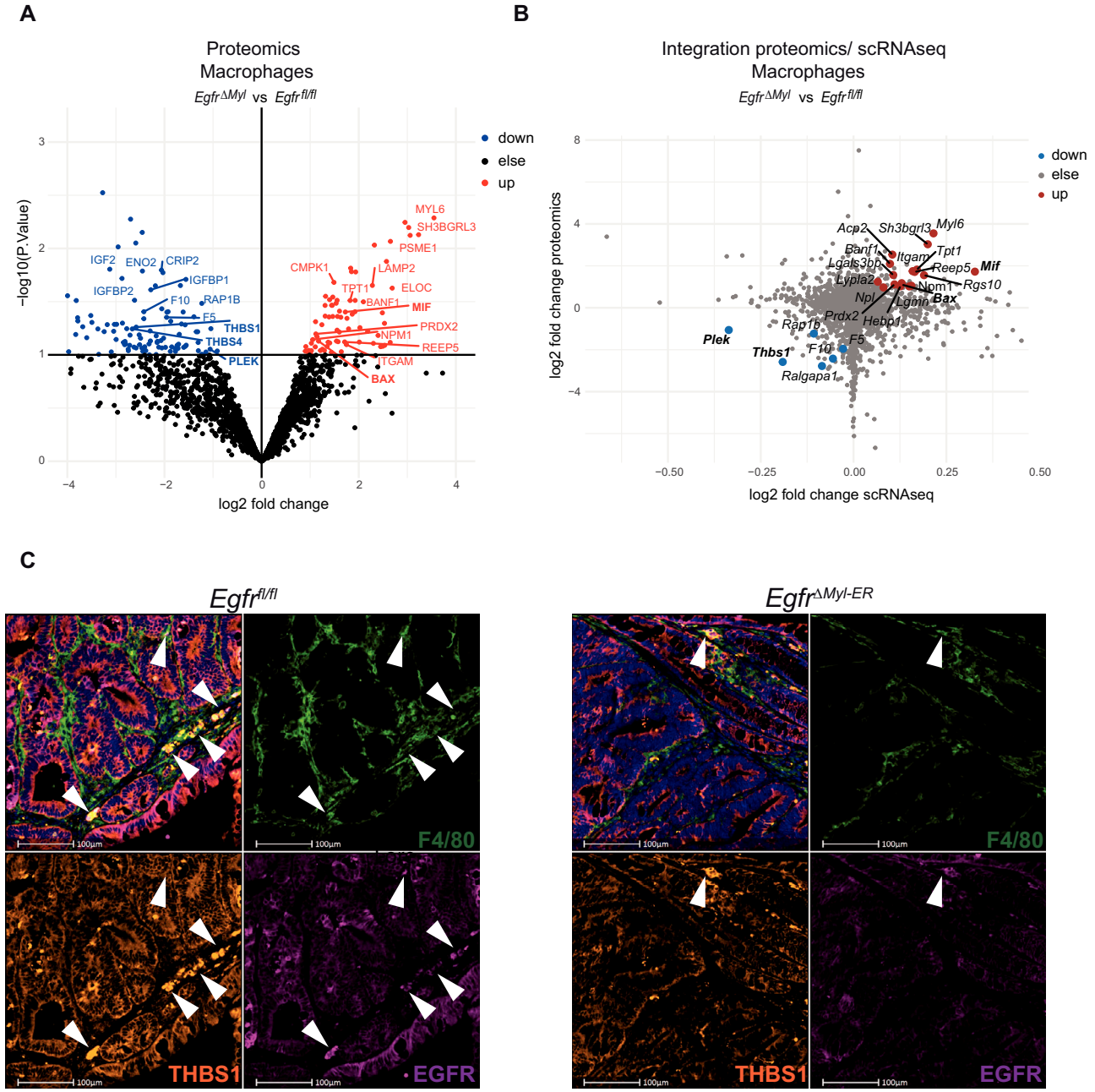


Fig. 6 Proteomic analysis of myeloid cells and comparison to scRNAseq reveals common targets in macrophages. A Volcano plot of differentially expressed proteins detected by nano-flow mass spectrometry of FACS-sorted macrophages from $Egfr^{\Delta Myl}$ and $Egfr^{fl/fl}$ tumors ($Egfr^{fl/fl}$, $n = 2$; $Egfr^{\Delta Myl}$, $n = 2$, $P < 0.1$). **B** Correlation plot of up- and down-regulated genes (scRNAseq, $Padj < 0.05$) and proteins (proteomics, $P < 0.1$) of $Egfr^{\Delta Myl}$ *vs* $Egfr^{fl/fl}$ macrophages isolated from AOM/DSS tumors. **C** Co-immunostaining for F4/80, THBS1, and EGFR in $Egfr^{fl/fl}$ *and* $Egfr^{\Delta Myl\text{-}ER}$ AOM/DSS tumors. Arrowheads indicate triple-positive cells.

stage II and III CRC samples (Table S11) [35]. First, these patients were stratified into high or low *EGFR*-expressing groups. Survival analysis then showed that high *EGFR* expression did not significantly impact the outcome compared to low *EGFR* expression (Fig. 7D) ($P = 0.1$, log-rank test). *THBS1*, which we identified as a robust proxy for EGFR activity in myeloid cells in both mouse and human datasets (Figs. 3H, 6B, and 7B), instead showed a significant prognostic value. High *THBS1* expression was associated with a worse survival outcome (Fig. 7D) ($P = 0.0014$, log-rank test). A combined analysis of both *EGFR* and *THBS1* revealed a synergistic effect for only a few patients, and patients with high expression for both genes exhibited even slightly worse outcomes (Fig. 7D) ($P = 0.0014$, log-rank test).

Next, we aimed to test whether signatures for the macrophage or granulocyte subsets that we identified in our murine model have prognostic value for overall survival in CRC patients. Therefore, we used the top markers driving the clusters of $C1qc^{+}$, $Spp1^{+}$ macrophages, and those of the $S100a9^{+}$ neutrophils. The $C1qc^{+}$ signature genes showed the strongest correlation in the human CRC data (Fig. S7A). We then conducted GSVA to stratify CRC patients into a high (Sig^{high}) and a low (Sig^{low}) expression group. Elevated expression of all three myeloid signatures correlated with poorer survival outcomes, indicating that enrichment of such myeloid populations in human primary CRC is associated with worse prognosis (Figs. 7E, F and S7B) ($P < 0.021$, log-rank test). Low expression of *EGFR* synergized with

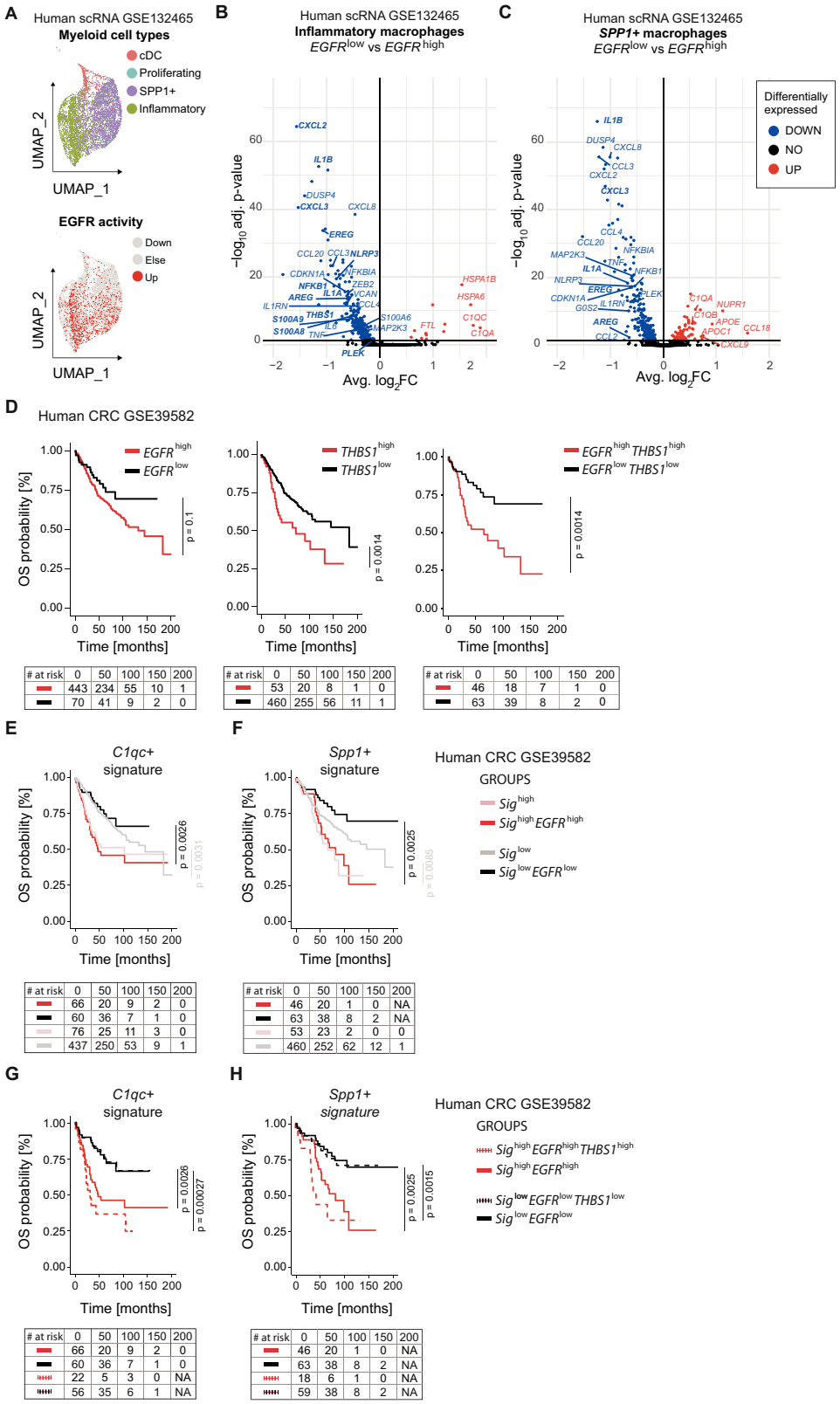


Fig. 7 EGFR pathway is active in pro-inflammatory and *SPP1*$^{+}$ myeloid cells in human CRC. A UMAP showing EGFR pathway activity in myeloid cell clusters of human CRC, detected by scRNAseq and PROGENy. Volcano plots of differential gene expression of *EGFR*^{low} vs *EGFR*^{high} signaling based on PROGENy-calculated scores in **B** inflammatory and **C** *SPP1*$^{+}$ macrophage clusters. Color coding indicates significantly altered genes (*Padj* < 0.05). **D** Kaplan-Meier plots showing overall survival (OS) associated with *EGFR* and/or *THBS1* expression in human bulk CRC tumors. Kaplan-Meier plots showing overall survival associated with *EGFR* and myeloid signature expression (Sig) for **E** *C1qc*$^{+}$ macrophages, and **F** *Spp1*$^{+}$ macrophages. Clinical outcomes associated with *EGFR*, myeloid signatures (Sig), and *THBS1* expression for **G** *C1qc*$^{+}$ macrophages, and **H** *Spp1*$^{+}$ macrophages. The log-rank test was used to test for significance in survival plots.

a low expression of *C1qc*$^+$, *Spp1*$^+$ macrophage or *S100a9*$^+$ neutrophil signatures, while exhibiting the highest overall survival probability for CRC patients (Figs. 7E, F, and S7B) ($P < 0.0051$, log-rank test). However, high co-expression of EGFR and myeloid signatures did not correlate with worse survival outcomes compared to myeloid signatures alone (Figs. 7E, F and S7B).

To further evaluate the potential synergistic effects of *EGFR*, *THBS1*, and the myeloid signatures, we integrated *THBS1* into the respective signatures and then reassessed the survival within these subgroups. Concomitant high expression of *THBS1*, EGFR, and the macrophage signatures *C1qc*$^+$ and *Spp1*$^+$ showed a slight negative influence on the survival outcomes of CRC patients (Fig. 7G, H). However, the same negative trend was not observed in conjunction with the neutrophil signatures (Fig. S7C). Importantly, both the *C1qc*$^+$ and *Spp1*$^+$ triple high macrophage signature combinations were independent adverse prognostic factors for relapse-free survival (RFS) and they were not influenced by the tumor stage, adjuvant chemotherapy status, age, sex, and *KRAS* mutation status, while they correlated with a worse RFS (Fig. S7D–G).

Adverse prognostic value of the *Spp1*$^+$ triple signature was further shown when we pooled adjusted hazard ratios from multiple independent CRC cohorts using random effects models. In the overall population of analyzed CRC patients, the pooled hazard ratio for the *Spp1*$^+$ triple signature was 1.41 (95% CI 1.04–1.91, $P = 0.02$, $I^2 = 0\%$) (Fig. S8A). In stage-stratified analyses, the *Spp1*$^+$ signature was associated with worse survival outcomes in stage III (OS: pooled HR = 1.64, 95% CI 1.01–2.65, $P = 0.04$; PFS/RFS: pooled HR = 1.92, 95% CI 1.10–3.33, $P = 0.02$; $I^2 = 0\%$ for both) (Fig. S8B, C). Together, we showed that *Spp1*$^+$ triple high signature is a robust independent adverse prognostic factor for CRC.

Importantly, we demonstrated the presence of C1QC$^+$ macrophages (CD68$^+$) co-expressing EGFR and THBS1 in the stroma of human CRC (Fig. 8A). Additionally, we used an available human CRC cohort combining whole-transcriptome spatial molecular imaging with single-nucleus RNA-sequencing to identify CD68$^+$ macrophages within the TME (Fig. 8B, area of yellow polygon) [36]. Within this area, we could additionally detect transcripts for *C1QC*, *SPP1*, *EGFR*, and *THBS1* (Fig. 8C), confirming that macrophages co-expressing these markers are found in the TME of human CRC.

In summary, these results suggest that our findings from the AOM/DSS-induced tumors in mice are relevant to human CRC, and that a stronger presence of *C1qc*$^+$, *Spp1*$^+$ macrophages, and *S100a9*$^+$ neutrophils correlates with worse prognosis in CRC patients. In particular, our results highlight a strong correlation of *C1qc*$^+$ and *Spp1*$^+$ macrophages in conjunction with high expression of *EGFR* and *THBS1* with poor survival outcomes for CRC patients.

DISCUSSION

In this study, we show how EGFR signaling in myeloid cells shapes their phenotype and affects the overall composition of the CRC TME. By performing an unbiased scRNAseq analysis of tumors in mice with conditional deletion of EGFR in myeloid cells, we demonstrate an altered immune cell infiltration and a less immunosuppressive TME, accompanied by reduced activation of inflammatory signaling pathways in myeloid cells, impacting their communication with T cells. Importantly, we identify myeloid-derived *Thbs1* as a mediator affected by EGFR signaling and highlight its prognostic role in human CRC survival. Importantly, our preclinical study demonstrates that deletion of EGFR in myeloid cells within established colorectal tumors leads to a reduction in tumor size (Fig. S9). These findings strongly suggest that targeting EGFR specifically in myeloid cells may be of great therapeutic benefit for patients with CRC.

EGFR inhibition is the standard of care for patients with metastatic CRC carrying wild-type *KRAS*. However, not all patients benefit from this treatment, and the overall expression of EGFR in CRC tumors does not predict therapeutic outcomes, highlighting an incomplete understanding of how EGFR inhibitors exert their effects. Thus, a deeper mechanistic understanding is necessary for improved patient stratification and therapy success [37]. We and others have demonstrated a tumor-promoting role for EGFR-positive myeloid cells in cancer patients and CRC mouse models, suggesting that the therapeutic efficacy of EGFR inhibitors may be driven by their action on myeloid cells [8, 10].

In several tumor entities, the TME is dominated by TAMs, and their presence is often associated with a poor prognosis [38, 39]. In recent years, scRNAseq studies have revealed distinct TAM subpopulations associated with different outcomes in CRC, shifting the focus away from the classical M1-M2 dichotomy toward a spectrum of intermediate phenotypes within the TME [17, 40, 41]. Using scRNAseq and flow cytometry, we detected reduced numbers of F4/80^{hi} macrophages and LY6C^{hi} monocytes in *Egfr*$^{\Delta Myl}$ AOM/DSS tumors, whereas the number of neutrophils remained unchanged. A decrease of F4/80$^+$ macrophages was also confirmed in *Egfr*$^{Myl\text{-}ER}$ when EGFR was deleted in developed AOM/DSS tumors. Reduced numbers of CD68$^+$ macrophages had previously also been observed upon myeloid EGFR deletion in AOM/DSS tumor sections [10]. Unsupervised clustering of our scRNAseq data identified a reduction of the *Spp1*$^+$ and *C1qc*$^+$ macrophage subpopulations in tumors of *Egfr*$^{\Delta Myl}$ mice. The reduced numbers may be attributed to impaired differentiation from myeloid progenitors or decreased recruitment into the TME. While differentiation pathways did not show significant changes between wild-type and *Egfr*$^{\Delta Myl}$ macrophages and monocytes, several migratory and chemotactic signaling pathways were reduced in the absence of EGFR. We also observed reduced *Ccr1* levels in *Egfr*$^{\Delta Myl}$ monocytes and macrophages. In fact, altered recruitment of these cells had previously been attributed to CCR1 inhibition [42]. Thus, the downregulation of migration-related pathways highlights EGFR as a key factor for *Spp1*$^+$ and *C1qc*$^+$ macrophage recruitment in CRC tumors. Interestingly, recent studies showed that patients with *SPP1*^{hi} or *C1QC*^{hi} TAMs showed worse clinical outcomes [12, 43–45]. Moreover, *C1QC* macrophages express high levels of *ADGRE1*, encoding F4/80 in mice, and are associated with phagocytosis, complement proteins, and antigen presentation [17]. In contrast, *SPP1* macrophages express angiogenic genes and have been connected to TGFβ and IL1 signaling [12]. Thus, EGFR deletion in myeloid cells might relieve immunosuppression by reducing the infiltration of *Spp1*$^+$ and *C1qc*$^+$ macrophages into the tumors.

We also demonstrated that both macrophage clusters were not only reduced in numbers but also showed downregulation of a broad range of diverse inflammatory cytokines such as TGFβ, IFNγ, and IL6. Previous findings from our laboratory had reported reduced IL6 expression in EGFR-deficient Cd11b$^+$ myeloid cells [8, 9]. High TGFβ signaling has been shown to promote angiogenesis, metastasis, and T_{reg} cell differentiation [45]. These tumor-promoting mechanisms might therefore be reduced in *Egfr*$^{\Delta Myl}$ tumors. Moreover, reduced IFNγ signaling may be responsible for the reduced expression of checkpoint genes like *Lilrb4a* or *CD274* (PDL1), as the latter has been shown to be regulated by IFNγ [46]. Therefore, impaired macrophage infiltration, along with decreased expression of tumor-promoting inflammatory cytokines, may explain why EGFR deletion in myeloid cells results in reduced tumor growth.

EGFR deficiency in myeloid cells also affects downstream signaling pathways. Using PROGENy, we detected the highest EGFR activity among myeloid cell clusters in wild-type *S100a9*$^+$ neutrophils and *Spp1*$^+$ macrophages. EGFR deletion induced the strongest reduction in EGFR-related pathways in *Spp1*$^+$ macrophages and DC subpopulations, and to a lesser extent in *C1qc*$^+$ TAMs, resulting in reduced JAK/STAT and PI3K/AKT pathway activity in these cells. The JAK/STAT pathway is essential for the

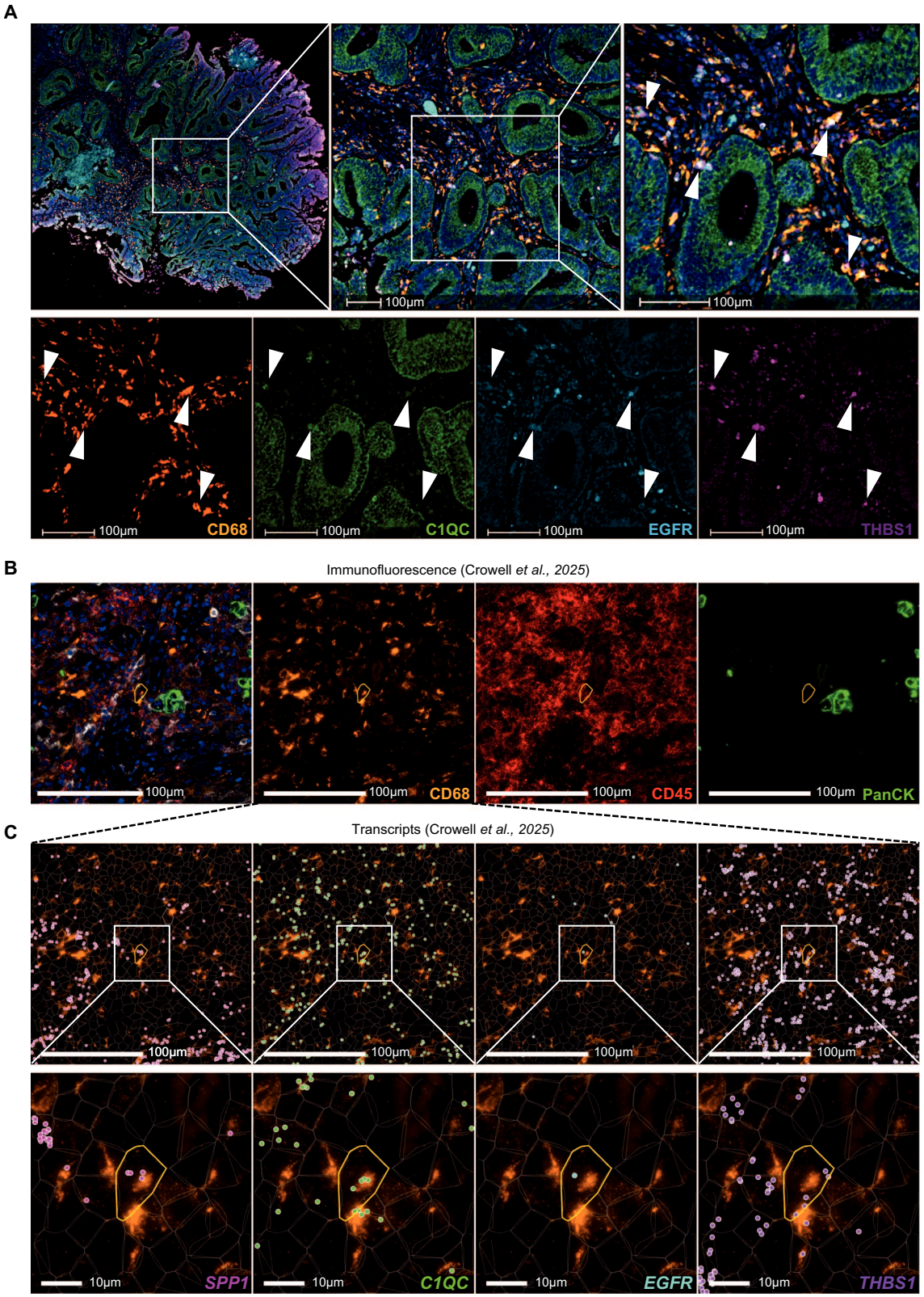


Fig. 8 Co-expression of EGFR, C1QC, SPP1, and THBS1 in CD68$^+$ macrophages in the TME of human CRC. A Multiplex immunofluorescence staining of human CRC. Staining panel included antibodies against CD68, C1QC, EGFR, and THBS1. DAPI was used for nuclei detection. Magnification: x3, x5, x20. Scale bars: 1 mm and 100 µm. Arrowheads indicate macrophages triple-positive for C1QC, EGFR, and THBS1. **B** Immunofluorescence staining for the indicated markers of human CRC samples reported by Crowell et al. 2025 (WTx CosMx SMI data): DAPI, B2M/CD298 (white), CD68, CD45, and PanCK. The yellow polygon indicates the macrophage of interest analyzed for the presence of *EGFR*$^+$ *THBS1*$^+$ *SPP1*$^+$ *C1QC*$^+$ RNA transcripts. **C** Spatial maps of RNA transcripts *SPP1*, *C1QC*, *EGFR*, *THBS1* overlaying on immunofluorescence images showing the CD68 channel only and polygons indicating cell boundaries. The yellow polygon indicates the macrophage of interest. Scale bars: 100 µm and 10 µm.

expression of IFN-stimulated genes, including some checkpoint molecules [47]. STAT3 activation in myeloid cells has also been correlated with macrophage polarization and worse prognosis for cancer patients [48, 49]. Moreover, it has also been shown to promote tumor growth in the AOM/DSS model [50]. The PI3K pathway is also an important regulator of myeloid cell functions, influencing, among others, their polarization and migration into tumors [51–53].

Growth factors such as EGF or TGFβ produced by tumor cells can modulate macrophage polarization via PI3K [54, 55]. Along these lines, PI3K blockade has been shown to reduce immune suppression by changing the expression of genes, including *Thbs1* [53]. Thus, our data indicate that a lack of EGFR signaling in macrophages results in reduced activation of downstream pathways such as JAK/STAT and PI3K, influencing the expression of important immune mediators, possibly affecting other cells in the TME.

T cell migration, differentiation, and activation are primarily driven by DCs and macrophages [56]. T cell differentiation and infiltration of T_{regs} contribute to immunosuppression in CRC, while blockade of T_{reg} differentiation leads to decreased tumor burden in the colon [57, 58]. The reduced activation of the TGFβ pathway observed in *C1qc*$^+$ and *Spp1*$^+$ macrophages may contribute to the decreased T_{reg} cell numbers in *Egfr*$^{\Delta Myl}$ tumors, which in turn could lead to a reduced tumor burden. Interestingly, computational analysis of cell-to-cell interactions in our scRNAseq dataset indicates an altered crosstalk between myeloid cells and T cells, involving checkpoint ligand-receptor interactions. Upon EGFR deletion, the probabilities for interactions of checkpoint and cytokine ligand-receptor pairs associated with T cell suppression were decreased, suggesting again that EGFR signaling in myeloid cells supports T cell-mediated immunosuppression.

Tumor-infiltrating macrophages play a role in the induction of T cell exhaustion, which often correlates with poor prognosis [59, 60]. In our cohort, we detected reduced expression of the exhaustion molecules *Pdcd1* and *Havcr2* on CD8$^+$ T cells in *Egfr*$^{\Delta Myl}$ tumors. This coincided with reduced *Ifngr1* expression in CD8 T cells and reduced IFN II signaling in macrophages lacking EGFR. In line with our observations, it was recently demonstrated that chronic IFNγ signaling activation in cytotoxic T cells limits anti-tumor responses through decreased generation of T cells with intermediate exhaustion marker expression [61]. Taken together, these results reflect a potentially less immunosuppressive state for T cells in murine CRC tumors lacking EGFR in myeloid cells.

By integrating transcriptomic and proteomic data, we demonstrate a reduction in THBS1 expression in F4/80^{hi} *Egfr*$^{\Delta Myl}$ macrophages, consistent with the observed downregulation of the TGFβ pathway. Notably, the difference was more pronounced at the protein than at the transcript level, potentially reflecting post-transcriptional and/or post-translational regulation, as well as methodological differences among scRNAseq and LC–MS/MS. Importantly, immunostaining confirmed co-expression of THBS1 and EGFR in TAMs, further supporting a link between myeloid EGFR signaling and THBS1 protein abundance within the TME. Recent work identified infiltrating tumor monocyte-like cells and macrophages as the main source of THBS1, linking its expression to increased metastatic potential and poorer patient outcomes [62]. In line with these observations, we show that high *THBS1* expression is associated with worse survival outcomes in a CRC patient cohort. Furthermore, using myeloid signatures identified in our murine model, we found that co-expression of a high *EGFR*, *THBS1*, and *C1qc*$^+$ macrophage signature correlates with worse overall survival in patients. Consistently, analysis of a human CRC scRNAseq dataset revealed that low EGFR activity was associated with reduced *THBS1* expression in pro-inflammatory macrophages. Our results suggest that myeloid-derived THBS1 likely serves as a key ligand in T cell communication, which is downregulated in myeloid cells of *Egfr*$^{\Delta Myl}$ tumors. Notably, predicted cell-cell interaction analysis revealed that, alongside macrophages, neutrophils also contribute to THBS1 production, highlighting the TME complexity and the need for further investigation.

Functional in vivo evidence further supports the biological relevance of the EGFR-THBS1 axis identified in our study. Omatsu et al. demonstrated that myeloid-specific *Thbs1* deletion using the LysM-Cre line (the same strategy we used here for myeloid-specific *Egfr* deletion) significantly reduced metastatic burden in an orthotopic implantation model using murine tumor organoids (MTOs) [62]. In the same study, the authors also showed that TME-derived THBS1 promotes cytotoxic T-cell dysfunction/exhaustion in CRC, and ex vivo THBS1 administration promoted the expression of exhaustion-associated markers in T cells and suppressed cytotoxic activity of T cells [62]. Although this work did not assess EGFR signaling, it provides in vivo evidence that monocyte/macrophage-derived THBS1 contributes to CRC progression, strongly supporting our findings. Collectively, these data suggest that myeloid EGFR signaling, potentially via THBS1-associated pathways, promotes immunosuppression in CRC and may affect responsiveness to immunotherapy. In future studies, targeted delivery strategies (e.g., nanoparticles directed to EGFR$^+$F4/80$^+$ macrophages) could enable myeloid-specific EGFR inhibition while limiting off-target effects and supporting combination with immune checkpoint inhibitors. Together, these findings establish a link between macrophage EGFR signaling, *THBS1* expression, and patient prognosis and suggest that myeloid-derived THBS1 may serve as a potential biomarker for future patient stratification, emphasizing the clinical relevance of our findings.

MATERIALS AND METHODS

Mouse experiments and human material

Egfr$^{fl/fl}$ mice [63] were crossed with *LysM*-Cre mice [64], tamoxifen (Tx)-inducible *LysM-CreER*, or *Cd11c*-Cre mice [65]. Detection of *Egfr*^{fl} and *Egfr*$^{\Delta}$ alleles was performed by PCR, using the primers R4 (GCCTGTGTCCGGGTCTCGTCG), R6 (CAACCAGTGCACCTAGCCTGG), and *Egfr*-fwd (AAGTTTAAG). Experiments were performed using mice 8-12 weeks of age. The sample size was chosen according to previously published experimental setups [8]. Human CRC material, used for multiplex immunofluorescence, was obtained from the Department of General Surgery at the Medical University of Vienna.

Tumorigenesis

Briefly, mice were injected intraperitoneally with AOM, females with 12.5 and males with 10 mg/kg (A5486; Sigma-Aldrich, St. Louis, MO), followed by regular diet and water for 5 days. Mice then received 2.5% DSS (02160110-CF; MP Biomedicals, Santa Ana, CA) in autoclaved water for 5 days, followed by maintenance on regular autoclaved water for 16 days and two additional DSS cycles (5 days of 2.5% DSS and 5 days of 2% DSS). Mice were sacrificed 30 days after the last DSS treatment.

For inducible EGFR deletion in established tumors, mice were fed a tamoxifen diet (GENOdiet CreActive T400, GEN16/T400-R; Genobios) until the end of the experiment.

Peritoneal cell isolation

Peritoneal macrophages were isolated as previously described [66]. Briefly, peritoneal lavage was performed with 10 ml PBS (D8537; Sigma-Aldrich) containing 2 mM EDTA (8040.2; Roth Calbiochem). The resulting cell suspension was centrifuged for 6 min at 300 × *g* at 4 °C. Cells were plated in RPMI-1640 medium (R8758; Sigma-Aldrich) supplemented with 10% fetal calf serum (FCS; F7524, Sigma-Aldrich) and 1% penicillin/streptomycin (P4333; Sigma-Aldrich) and washed after 60 min.

Magnetic cell sorting

For isolation of DCs from spleen, we performed positive magnetic cell sorting using a biotinylated Cd11c antibody (N418; BioLegend) and IMag streptavidin particles (557812; BD Biosciences), according to the manufacturer's instructions. Sorting quality was assessed by flow cytometric analysis, revealing that most sorted live cells were CD45$^+$/ CD11c$^+$.

Flow cytometry and cell sorting

Colon polyps were cut into pieces and digested in RPMI medium supplemented with 10% fetal calf serum (FCS), 1% penicillin/streptomycin, 1.5 mg/ml Collagenase VIII (C2139; Sigma-Aldrich) and 0.5 mg/ml DNase I (D5319; Sigma-Aldrich) for 1 h at 37 °C, shaking at 300 rpm. Samples were filtered through a 70-µm cell strainer and washed once with Hank's balanced salt solution (H6648; Sigma-Aldrich) containing 10% FCS, 1% penicillin/streptomycin, and 5 mM EDTA and twice with PBS containing 5% FCS, 5 mM EDTA, and 20 µg/ml DNase I. Cell suspensions were initially blocked with Fc-block (CD16/CD32, 101301; BioLegend) following staining with fluorescent antibodies for 30 min at 4 °C. Used antibodies are listed in Table S12. Data were acquired using an LSRFortessa flow cytometer (BD Biosciences) and analyzed with FlowJo software v10.6 (FlowJo, LLC, Ashland, OR). Appropriate gating strategies were applied for fluorescence-activated cell sorting and cells were resuspended in RPMI supplemented with 2 mM EDTA and 20 µg/ml DNase I. Cells were sorted into TRIzol LS Reagent (10296010; Thermo Fisher Scientific) for RNA isolation or into RPMI supplemented with 50% FCS for protein isolation with a FACSAria III (BD Biosciences).

Intracellular staining

For the detection of intracellular antigens, cells were stained for external antigens and subsequently fixed and permeabilized using the Foxp3/Transcription factor staining set (00-5523; Thermo Fisher Scientific) according to the manufacturer's instructions.

Immunofluorescence and multiplex immunofluorescence

Paraffin sections with a thickness of 4 µm were prepared for immunofluorescence by deparaffinizing them through incubation at 65 °C for 15 min, followed by rehydration using an alcohol series according to standard protocols.

For immunofluorescence staining of mouse CRC tumor sections, antigen retrieval was performed at pH 9.0. Samples were blocked with a mouse on mouse kit (M.O.M MKB-2213-1; Vector Laboratories) to prevent nonspecific binding and incubated overnight with primary antibodies for F4/80, EGFR, and THBS1.

For multiplex immunofluorescence, samples were blocked with 2% BSA, 5% horse serum and 0.1% Triton in PBS. To detect multiple tissue markers, we used the Opal 6-Plex Detection kit (NEL811001KT, Akoya Biosciences) according to the manufacturer's instructions. Briefly, tissue sections were incubated with primary antibodies for 1 h at room temperature (RT), followed by incubation with the secondary HRP-coupled antibody (10 min, RT). Slides were then stained with the appropriate Opal Fluorophore (10 min, RT). Microwave treatment was used to remove the primary–secondary HRP complex. This process was repeated up to four times to detect respective tissue markers. Finally, samples were counterstained with 4,6-diamidino-2-phenylindole (DAPI) to visualize the nuclei. The antibodies used are listed in Table S12. Slides were scanned with VS200 Slidescanner (Evident) and analyzed using HALO software (Indica Labs, v4.1).

Quantitative reverse transcription

Total RNA isolation was performed from peritoneal macrophages and DCs with TRIzol (15596026; Invitrogen) according to the manufacturer's protocol. Complementary DNA (cDNA) synthesis was performed using SuperScript VILO Master Mix (11756050; Invitrogen). FACS-sorted myeloid cells were sorted into TRIzol LS Reagent (10296010; Invitrogen), and RNA was isolated using the miRNeasy Micro Cleanup Kit (217084; Qiagen). For cDNA synthesis, LunaScript RT SuperMix (NEB #E3010; New England BioLabs) was used.

TaqMan Gene Expression Assays (*Egfr* FAM: Mm01187858_m1; *Tbp* VIC: Mm01277042_m1 and *Hprt* VIC: Mm03024075_m1, Thermo Fisher Scientific) and TaqMan™ Fast Advanced Master Mix for qPCR (4444557; Applied Biosystems™) were used for quantitative real-time PCR (qRT-PCR) according to the manufacturer's instructions and performed on a real-time PCR system (CFX96 Touch System, Bio-Rad). Fold changes between genotypes were calculated using the ΔΔCt method, with *Tbp* (TATA box binding protein) and *Hprt* (hypoxanthine guanine phosphoribosyl transferase) as reference genes.

Western blot

Cells were lysed in appropriate buffers using standard protocols [67]. Protein lysates were resuspended in the appropriate loading buffer by SDS-PAGE and transferred to nitrocellulose PVDF membranes (GE10600023; Merck). The following primary antibodies were used: EGFR (71655; Cell Signaling) and HSP90 (4874; Cell Signaling), overnight at 4 °C, followed by horseradish peroxidase (HRP)-conjugated secondary antibodies for 60 min at room temperature. Enhanced chemiluminescence (ECL; GERPN2235; Merck) and Chemi-Doc gel imaging system (Bio-Rad) were used for development.

Single-cell sorting, library preparation, and sequencing of mouse CRC tumors (10x Genomics)

Colorectal tumors from three mice per group were pooled. Single-cell suspensions collected from CRC samples were stained with antibodies against CD45, CD326, CD11b, CD64, F4/80, and Gr-1 (as shown in Table S12) for FACS purification, which was performed to achieve a concentration of 800 cells per µl on a BD Aria III instrument.

Sorted $CD45^+$ and $CD45^-$ single-cell suspensions were loaded onto a Chromium Single Cell Chip (10x Genomics) according to the manufacturer's instructions for co-encapsulation with barcoded Gel Beads at a target capture rate of 10,000 individual cells per sample. Captured mRNA was barcoded during cDNA synthesis, and subsequent steps were carried out following the manufacturer's protocol using the Chromium Single Cell 3′ Solution v3.1 (10x Genomics). All tumor samples were processed simultaneously with the Chromium Controller (10x Genomics), and the resulting libraries were prepared in parallel to avoid batch effects. Final libraries were quality checked on a Tape Station (Agilent Technologies) using the HS D1000 tape. DNA concentration was determined using a Qubit analyzer (Thermo Fisher Scientific). All libraries were sequenced with an 8-base index read, a 26-base read 1 containing cell-identifying barcodes and unique molecular identifiers (UMIs), and a 98-base read 2 containing transcript sequences on an Illumina HiSeq 4000 instrument.

scRNAseq data processing and analysis

Alignment was performed using cellRanger (v3.0.2) on the raw data using the mm10 annotation. cellRanger aggr was used to aggregate samples. Filtering steps to remove low-quality cells, empty droplets, multiplets, and mitochondrial contamination were performed using functions from the Pagoda2 R package (v1.0.10) [68]. The gene.vs.molecule.cell.filter() function was applied to exclude cells with anomalously high gene counts (max.cell.size set to 5e4, and min.cell.size to 500). To assess mitochondrial contamination, the proportion of mitochondrial reads was calculated using the PercentageFeatureSet() function from the Seurat R package (v4) [69]. We defined the set of all genes starting with "MT-" as mitochondrial genes and discarded cells with over 20% of their counts mapping to them.

The following steps were all performed using the Seurat R package (v4) [69]. To account for differences in sequencing depth between cells, we used the NormalizeData() function, followed by the ScaleData() function. We then applied the FindVariableFeatures() function to identify the most variable features in the dataset using the variance-stabilizing transformation (VST) method. We selected the top 2000 variable genes. The four different samples were then integrated using the FindIntegrationAnchors() function.

To correct for potential variations in gene expression due to cells being in different phases of the cell cycle, we performed cell cycle regression using the CellCycleScoring() function. This algorithm estimates the cell cycle phase of each cell using a set of cell cycle marker genes, and then regresses out the cell cycle effect from the gene expression data. Specifically, we first calculated an S phase score and a G2M phase score (based on annotated genes). The algorithm then regressed out the cell cycle effect from the gene expression data using a linear regression model.

After running principal components analysis (PCA) on the most variable genes, UMAP embeddings were generated using the top 30 principal components and default parameters [70].

To cluster the cells, we applied graph-based clustering using the Louvain algorithm, using the function FindClusters() with a resolution of 0.5. FindNeighbors() was run with default parameters. Subclustering of myeloid and T cells to further resolve the heterogeneity of these cell types was run on these subsets, with the same approach and parameters.

Identification of EGFR, PI3K, and JAK/STAT signaling pathways using a PROGENy model and decoupleR package

The decoupleR R/Bioconductor package (v2.10.0) uses an ensemble of computational methods to infer biological activities from omics data [18]. We used the Weighted Mean method (wmean) to assess regulator

activities, which involves multiplying each target feature by its associated weight and summing the results to obtain an enrichment score. To obtain a *null* distribution, we performed permutations of random target features and used them to compute a *z*-score (norm_wmean) and a corrected estimate (corr_wmean) by multiplying wmean by the -log10 of the empirical P value obtained. Our analysis using the PROGENy R/Bioconductor package (v1.26.0) and the decoupleR package allowed us to identify signaling pathways that may be regulated by the EGFR signaling pathway in different cell types in our dataset, providing further understanding of the biological mechanisms underlying our data.

Receptor-ligand Interactions and cell communication network analysis

To investigate the network communication between different cells in our scRNAseq dataset, we used the R packages CellChat [29] and iTALK [30]. CellChat (v1) uses ligand-receptor pairs and gene expression data to predict intercellular signaling events and identify potential signaling pathways between cell types. To analyze the differential number of interactions or interaction strength among different cell types, we performed differential analysis. Significant signaling pathways were ranked based on differences in the overall information flow within the inferred networks between KO and WT.

We followed the standard CellChat (v1) workflow, which involved the following steps: (1) Loading the CellChatDB for cell-cell communication analysis. (2) Calling the createCellChat() method with the RNA data and metadata from the Seurat object. (3) Applying the identifyOverExpressedGenes() function to identify genes that are over-expressed in one cell population compared to others. (4) Compute the communication probability for each cell-cell interaction using computeCommunProb() function, and removing cell-cell interactions that involve fewer than 10 cells. (5) Aggregating the communication network by signaling pathway using the aggregateNet() function. (6) Visualizing the interaction network using netVisual_circle(), with plots showing the number of interactions and interaction weights/strength. (7) Visualizing significant interactions from specific cell groups using netVisual_bubble(), with the sources and targets specified as myeloid and T cells, respectively.

Receptor-ligand interactions were further investigated using iTalk (v0.1.0) [30]. Ligand-receptor pairs were selected based on the highest strength values. The strength of the prediction was calculated by the product of the mean expression of the ligand and receptor for the box plot or by the product of the $\log_2$ fold change of the ligand and receptor in the circos plots, as described in the iTalk package. The LRPlot() function was used for the circos plots, showing the predicted ligand-receptor pairs between myeloid and T cells. Only the top 50 interactions according to the highest strength values are displayed, with an *Padj* value < 0.05 for either the ligand or receptor. P value correction for multiple testing was done according to Benjamini-Hochberg.

Differential gene expression analyses between genotypes

Differential gene expression analyses were calculated using linear models, implemented in the R/Bioconductor package limma (v3.54.2) [71]. P value correction for multiple testing was done according to Benjamini-Hochberg [72].

Gene set variation analysis

GSVA was performed using the GSVA R/Bioconductor package (v1.46) [73]. Pathway and term-specific gene sets were obtained from the Molecular Signature Database (MSigDB) [74]. Gene expression values were transformed into gene set scores using the GSVA function with a Poisson distribution as a cumulative density function. Differences in GSVA scores were calculated using linear models, implemented in the R/Bioconductor package limma (v3.54.2) [71]. P value correction for multiple testing was done according to Benjamini-Hochberg [72].

Sample preparation for mass spectrometry

Sorted myeloid cells were washed once with cold PBS and resuspended in RIPA lysis buffer containing 25 mM trizma hydrochloride (Tris-HCl) ph=7.6 (T1503; Sigma-Aldrich), 1% w/v sodium deoxycholate (D6750; Sigma-Aldrich), 150 mM sodium chloride (NaCl; 1.06404; Sigma-Aldrich), 0.1% w/v sodium dodecyl sulfate (SDS; 1610418; Bio-Rad), 1% v/v nonidet NP-40 (N-6507; Sigma-Aldrich), supplemented with 1 mM sodium orthovanadate (Na_3VO_4; S6508; Sigma-Aldrich), 10 mM sodium fluoride (NaF; 7681-49-4; Thermo Fisher Scientific), 1 ug/ml Aprotinin (A1153-1MG; Sigma-Aldrich), 0.1 mg/ml 4-2-(aminoethyl) benzenesulfonylfluoride (AEBSF; 1248390500; Merck), 250 U Benzonase (70746-4; Sigma-Aldrich), 10 U DNAse I (DN25-1G; Scient Labo) and 1x PhosphoSTOP (4906845001; Sigma-Aldrich). Samples were incubated for 30 min at 4 °C and frozen in liquid nitrogen. Protein concentrations were determined by employing the Pierce BCA Protein Assay Kit (23227; Thermo Fisher). In total, 2 µg of protein per sample was used for further processing. The disulfide bonds of proteins were reduced with 40 mM Tris(2-carboxyethyl) phosphine (TCEP) and then alkylated with 10 mM chloroacetamide (CAA) for 60 min at 37 °C. Protein digestion and clean-up were performed using an adapted version of the automated paramagnetic bead-based single-pot, solid-phase-enhanced sample-preparation (Auto-SP3) protocol on the Bravo liquid handling platform (Agilent) [75]. Briefly, for bead preparation, Sera-Mag Speed Beads A and B (Cytiva) were vortexed until the pellet was dissolved. The suspension was placed on a magnetic rack, and after one minute, the supernatant was removed. The beads were taken off the magnetic rack and suspended in water. This procedure was repeated three times. A total of 10 µl of bead A was combined with 10 µl of bead B, and the final volume was corrected to 100 µl with H_2O. To each sample, a total of 5 µl of A + B beads was added. To induce the binding of the proteins to the beads, ethanol was added to each sample to a final concentration of 50% (v/v). Samples were then incubated for 15 min at room temperature and 800 rpm. After the incubation step, samples were placed again on a magnetic rack, and after one minute, the supernatant was removed. Samples were taken off the magnetic rack and suspended in 80% ethanol. This procedure was repeated three times. Finally, samples were reconstituted in 100 mM TEAB buffer containing trypsin (enzyme/protein ratio of 1:25) and digested overnight on a shaker at 37 °C and 1000 rpm. After digestion, the recovered peptides were dried by vacuum centrifugation (1300 rpm at 45 °C) and stored at −80 °C until use.

LC-MS/MS analysis

Nano-flow LC-MS/MS was performed by coupling an Ultimate 3000 HPLC (Thermo Fisher Scientific, USA) to an Orbitrap Exploris mass spectrometer (Thermo Fisher Scientific, Germany). Peptide samples were dissolved in 15 µl loading buffer (0.1% formic acid (FA), 2% ACN in MS-compatible H_2O), and 2 µl were injected for each analysis. The samples were loaded onto a pre-column (trap) at higher flowrates (PEPMAP 100 C18 5 µm, 0.3mmx5mm, Thermo Scientific), using a loading pump and then switched to an analytical column (100 µm × 30 cm, packed in-house with Reprosil-Pur 120 C18-AQ, 1.9 µm resin, Dr. Maisch) at a flow rate of 3 µl/min in 98% buffer A (0.1% FA in MS-compatible H_2O). After loading, peptides were separated using a 120 min gradient from 2% to 38% of buffer B (0.1% FA, 80% ACN in MS-compatible H_2O) at a flow rate of 350 nl/min. The Orbitrap Exploris 480 was operated in data-independent (DIA) mode, with a m/z range of 350–1400. Full scan spectra were acquired in the Orbitrap at 120,000 resolution after accumulation to the set target value of 300% (100% = 1e6) and maximum injection time of 45 ms. The full scans were followed by DIA scans. A total of 47 isolation windows were defined, with an m/z range of 406-986. DIA scan spectra were acquired at 30,000 resolution after accumulation to the set target value of 1000% (100%=1e5) and maximum injection time of 54 ms. Normalized collision energy (NCE) was set to 28%.

Database search and data analysis

All DIA–MS data files were analyzed with a directDIA workflow using Spectronaut 17.3 (Biognosys, Zurich, Switzerland). For the Pulsar search, the UniProt mouse-reviewed canonical reference proteome (20,404 entries, downloaded on December 7th, 2022) was used. The default settings for database match included full specificity trypsin digestion, peptide length of between 7 and 52 amino acids, and maximum missed cleavage of 2. N-terminal methionine was removed during the preprocessing of the protein database. Carbamidomethylation at cysteine was used as a fixed modification, and protein N-terminal acetylation and methionine oxidation were set as variable modifications. The false discovery rates (FDRs) were set to 0.01 for the peptide-spectrum match (PSM), peptide and protein identification. Other Spectronaut parameters for identification included maximum intensity as MZ extraction strategy, 0.01 precursor Qvalue Cutoff, 0.2 Precursor PEP Cutoff and stripped sequence as single hit definition. For quantification, the identified (Qvalue) was set for precursor filtering, MaxLFQ as protein LFQ method, and MS2 quantification with area as quantity type. For further analysis, only proteins without missing values were considered. For the analysis of the proteome data, the public server at usegalaxy.org was used [76]. Analysis was based on the R/Bioconductor

package limma (v3.5). Statistical testing of significance was performed using the voom() function [77].

Analysis of human data sets

Previously published scRNAseq data were accessed from the Gene Expression Omnibus (GEO) database under the accession number GSE132465 [19]. The raw matrix was filtered and normalized according to the criteria used by the authors, using the Seurat package (v4.1.1). Six major cell-type annotations and metadata were checked and further used. We implemented the PROGENy package (v1.26.0) through the decoupleR R/Bioconductor package (v2.10.0) to calculate the EGFR pathway activity, as described above. We then used the quantile() function to distinguish myeloid cells with low versus high EGFR activity. Differential gene expression of EGFR low versus high activity was calculated through the FindMarkers() function and the default Wilcoxon rank-sum test. A publicly available CRC cohort with raw gene expression data was accessed from the GEO database under the accession number GSE39582 [35]. After quality control and batch removal with the ArrayQualityMetrics R/Bioconductor package, a total of 516 CRC patient samples remained for subsequent analysis. The cut points for distinct patient groups in the survival analysis were defined with the survminer R package (v0.4.9). Maximum log-rank statistics were used to stratify patients into high and low gene-expressing groups. To predict the survival outcomes for CRC patients according to the gene signatures identified in our mouse 10x scRNAseq data, we used the top-expressed genes of the myeloid subclusters *C1qc*$^{+}$ macrophages, *Spp1*$^{+}$ macrophages, and *S100a9*$^{+}$ neutrophils. The GSVA R/Bioconductor package (v1.52.3) was used to estimate the enrichment scores for the three myeloid datasets, respectively. The gsvaParam() function was used with a Gaussian distribution as a cumulative density function, suitable for microarray data.

Whole-transcriptome spatial molecular imaging (WTx CosMx SMI) data of CRC patient samples, along with consecutive sections of immunofluorescence digital images, were previously reported by Crowell et al [36]. We re-analyzed the dataset using the processed cell-level data, matched cell boundary annotations, transcript coordinates, and immunofluorescence images provided with the published dataset release. *EGFR*$^{+}$ *THBS1*$^{+}$ macrophages were identified among filtered cells annotated as tumor-associated macrophages by requiring detectable expression of both *EGFR* and *THBS1*. Selected *EGFR*$^{+}$ *THBS1*$^{+}$ macrophages were then further checked for the detectable expression of *C1QC* (and/or *SPP1*), *EGFR*, and *THBS1* transcripts.

Survival analysis

The survival R package (v3.7.0) was used for the survival analyses, the log-rank test for statistical analysis between groups, and the corrplot R package (v0.94) for the gene correlation plots. Multivariable Cox proportional hazards regression was used to evaluate the independent prognostic value of the macrophage signatures in GSE39582, and in two additional independent CRC cohorts: CMC-BSN ($n = 185$) [78] and AC-ICAM ($n = 348$ mRNA-only, $n = 281$ with mutation data) [79]. Cox regression models were adjusted for pathological stage (III-IV vs I-II), adjuvant chemotherapy (not available for CMC-BSN), age (continuous), sex, and RAS mutation status. Subgroup analyses including only stage III patients were also performed. Forest plots displaying hazard ratios with 95% confidence intervals were plotted using the forestplot package (v3.1.7). We conducted random effects meta-analysis using the restricted maximum likelihood (REML) method on the adjusted hazard ratios of *C1qc*$^{+}$ or *Spp1*$^{+}$ triple signatures derived from Cox models fitted in each independent dataset. Meta-analysis was performed using the metafor package (v4.8-0) [80].

Statistics and figure design

GraphPad Prism 8 was used for statistical analysis. Data are given as mean ± SEM. Statistical significance was calculated by an unpaired Student's *t*-test to compare two experimental groups with similar variance, unless otherwise indicated. GraphPad calculator was used for the removal of statistically significant outliers. A P value of <0.05 was considered statistically significant ($^{*}P < 0.05$, $^{**}P < 0.01$, $^{***}P < 0.001$, $^{****}P < 0.0001$). Adobe Illustrator CS6 was used for figure creation and design.

DATA AVAILABILITY

Data can be accessed via the NCBI Gene Expression Omnibus repository under the accession number GSE279941. The proteomic data can be assessed at PRIDE under the accession number PXD058770. The relevant code of this study is available at Zenodo (https://doi.org/10.5281/zenodo.19197271) and GitHub (https://github.com/ReniaFari/EGFR_myeloid_CRC).

REFERENCES

1. Siegel RL, Wagle NS, Star J, Kratzer TB, Smith RA, Jemal A. Colorectal cancer statistics, 2026. CA Cancer J Clin. 2026;76:e70067.
2. Bray F, Laversanne M, Sung H, Ferlay J, Siegel RL, Soerjomataram I, et al. Global cancer statistics 2022: GLOBOCAN estimates of incidence and mortality worldwide for 36 cancers in 185 countries. CA Cancer J Clin. 2024;74:229–63.
3. Li J, Ma X, Chakravarti D, Shalapour S, DePinho RA. Genetic and biological hallmarks of colorectal cancer. Genes Dev; 2021;35:787–820.
4. Shah SC, Itzkowitz SH. Colorectal cancer in inflammatory bowel disease: mechanisms and management. Gastroenterology. 2022;162:715–30.
5. Dariya B, Aliya S, Merchant N, Alam A, Nagaraju GP. Colorectal cancer biology, diagnosis, and therapeutic approaches. Crit Rev Oncogenesis. 2020;25:71–94.
6. Venook AP, Niedzwiecki D, Lenz H, Innocenti F, Fruth B, Meyerhardt JA, et al. Effect of first-line chemotherapy combined with cetuximab or bevacizumab on overall survival in patients with Kras wild-type advanced or metastatic colorectal cancer: a randomized clinical trial. JAMA. 2017;317:2392–401.
7. Uribe ML, Marrocco I, Yarden Y. EGFR in cancer: signaling mechanisms, drugs, and acquired resistance. Cancers. 2021;13:2748.
8. Srivatsa S, Paul MC, Cardone C, Holcmann M, Amberg N, Pathria P, et al. EGFR in tumor-associated myeloid cells promotes the development of colorectal cancer in mice and associates with outcomes of patients. Gastroenterology. 2017;153:178–90.
9. Lanaya H, Natarajan A, Komposch K, Li L, Amberg N, Chen L, et al. EGFR has a tumour-promoting role in liver macrophages during hepatocellular carcinoma formation. Nat Cell Biol. 2014;16:972–81.
10. Hardbower DM, Coburn LA, Asim M, Singh K, Sierra JC, Barry DP, et al. EGFR-mediated macrophage activation promotes colitis-associated tumorigenesis. Oncogene. 2017;36:3807–19.
11. Deng H, Chen Y, Liu Y, Liu L, Xu R. Complement C1QC as a potential prognostic marker and therapeutic target in colon carcinoma based on single-cell RNA sequencing and immunohistochemical analysis. Bosn J Basic Med Sci. 2022;22:912–22.
12. Qi J, Sun H, Zhang Y, Wang Z, Xun Z, Li Z, et al. Single-cell and spatial analysis reveal interaction of FAP+ fibroblasts and SPP1+ macrophages in colorectal cancer. Nat Commun. 2022;13:1–20.
13. Baharom F, Ramirez-Valdez RA, Khalilnezhad A, Khalilnezhad S, Dillon M, Hermans D, et al. Systemic vaccination induces CD8+T cells and remodels the tumor microenvironment. Cell. 2022;185:4317–32.
14. Liu Y, Zhang Q, Xing B, Luo N, Gao R, Yu K, et al. Immune phenotypic linkage between colorectal cancer and liver metastasis. Cancer Cell. 2022;40:424–37.
15. Zhang L, Yu X, Zheng L, Zhang Y, Li Y, Fang Q, et al. Lineage tracking reveals dynamic relationships of T cells in colorectal cancer. Nature. 2018;564:268–72.
16. Abram CL, Roberge GL, Hu Y, Lowell CA. Comparative analysis of the efficiency and specificity of myeloid-Cre deleting strains using ROSA-EYFP reporter mice. J Immunol Methods. 2014;408:89–100.
17. Zhang L, Li Z, Skrzypczynska KM, Fang Q, Zhang W, O'Brien SA, et al. Single-cell analyses inform mechanisms of myeloid-targeted therapies in colon cancer. Cell. 2020;181:442–59.
18. Badia-I-Mompel P, Velez Santiago J, Braunger J, Geiss C, Dimitrov D, Muller-Dott S, et al. decoupleR: ensemble of computational methods to infer biological activities from omics data. Bioinform Adv. 2022;2:vbac16.
19. Lee HO, Hong Y, Etlioglu HE, Cho YB, Pomella V, Van den Bosch B, et al. Lineage-dependent gene expression programs influence the immune landscape of colorectal cancer. Nat Genet. 2020;52:594–603.
20. Cheng S, Li Z, Gao R, Xing B, Gao Y, Yang Y, et al. A pan-cancer single-cell transcriptional atlas of tumor-infiltrating myeloid cells. Cell. 2021;184:792–809.
21. Liu Y, Liu X, Xu Q, Gao X, Linghu E. A prognostic model of colon cancer based on the microenvironment component score via single-cell sequencing. Vivo. 2022;36:753–63.
22. Yamakita Y, Matsumura F, Lipscomb MW, Chou P, Werlen G, Burkhardt JK, et al. Fascin1 promotes cell migration of mature dendritic cells. J Immunol. 2011;186:2850–9.
23. Saichi M, Ladjemi MZ, Korniotis S, Rousseau C, Ait Hamou Z, Massenet-Regad L, et al. Single-cell RNA sequencing of blood antigen-presenting cells in severe COVID-19 reveals multi-process defects in antiviral immunity. Nat Cell Biol. 2021;23:5 2021;23:538-51.
24. Zhang J, Raper A, Sugita N, Hingorani R, Salio M, Palmowski MJ, et al. Characterization of Siglec-H as a novel endocytic receptor expressed on murine plasmacytoid dendritic cell precursors. Blood. 2006;107:3600–8.

25. Noe JT, Mitchell RA. MIF-dependent control of tumor immunity. Front Immunol. 2020;11:609948.
26. Van den Eynde M, Mlecnik B, Bindea G, Fredriksen T, Church SE, Lafontaine L, et al. The Link between the multiverse of immune microenvironments in metastases and the survival of colorectal cancer patients. Cancer Cell. 2018;34:1012–26.
27. Andreatta M, Corria-Osorio J, Muller S, Cubas R, Coukos G, Carmona SJ. Interpretation of T cell states from single-cell transcriptomics data using reference atlases. Nat Commun. 2021;12:2965.
28. Szabo PA, Levitin HM, Miron M, Snyder ME, Senda T, Yuan J, et al. Single-cell transcriptomics of human T cells reveals tissue and activation signatures in health and disease. Nat Commun. 2019;10:4706.
29. Jin S, Guerrero-Juárez CF, Zhang L, Chang I, Ramos R, Kuan C, et al. Inference and analysis of cell-cell communication using CellChat. Nat Commun. 2021;12:1 2021;12:1–20.
30. Wang Y, Wang R, Zhang S, Song S, Jiang C, Han G, et al. iTALK: An R Package to Characterize and Illustrate Intercellular Communication. Preprint at https://doi.org/10.1101/507871 2019.
31. Zhang N, Czepielewski RS, Jarjour NN, Erlich EC, Esaulova E, Saunders BT, et al. Expression of factor V by resident macrophages boosts host defense in the peritoneal cavity. J Exp Med. 2019;216:1291–300.
32. Zhu Y, Sun X, Tan S, Luo C, Zhou J, Zhang S, et al. M2 macrophage-related gene signature in chronic rhinosinusitis with nasal polyps. Front Immunol. 2022;13:1047930.
33. Zhao Y, Xiong Z, Lechner EJ, Klenotic PA, Hamburg BJ, Hulver M, et al. Thrombospondin-1 triggers macrophage IL-10 production and promotes resolution of experimental lung injury. Mucosal Immunol. 2014;7:440–8.
34. Chauhan D, Bartok E, Gaidt MM, Bock FJ, Herrmann J, Seeger JM, et al. BAX/BAK-induced apoptosis results in caspase-8-dependent IL-1β maturation in macrophages. Cell Rep. 2018;25:2354–68.
35. Marisa L, de Reynies A, Duval A, Selves J, Gaub MP, Vescovo L, et al. Gene expression classification of colon cancer into molecular subtypes: characterization, validation, and prognostic value. PLoS Med. 2013;10:e1001453.
36. Crowell HL, Ruano I, Hu Z, Hong Y, Caratù G, Piessevaux H, et al. Tracing colorectal malignancy transformation from cell to tissue scale. Preprint at https://doi.org/10.1101/2025.06.23.660674 2025.
37. Linardou H, Dahabreh IJ, Kanaloupiti D, Siannis F, Bafaloukos D, Kosmidis P, et al. Assessment of somatic k-RAS mutations as a mechanism associated with resistance to EGFR-targeted agents: a systematic review and meta-analysis of studies in advanced non-small-cell lung cancer and metastatic colorectal cancer. Lancet Oncol. 2008;9:962–72.
38. Bied M, Ho WW, Ginhoux F, Bleriot C. Roles of macrophages in tumor development: a spatiotemporal perspective. Cell Mol Immunol. 2023;20:983–92.
39. Mantovani A, Allavena P, Marchesi F, Garlanda C. Macrophages as tools and targets in cancer therapy. Nat Rev Drug Discov. 2022;21:799–820.
40. Peng J, Sun B, Chen C, Zhou J, Chen Y, Chen H, et al. Single-cell RNA-seq highlights intra-tumoral heterogeneity and malignant progression in pancreatic ductal adenocarcinoma. Cell Res. 2019;29:725–38.
41. Azizi E, Carr AJ, Plitas G, Cornish AE, Konopacki C, Prabhakaran S, et al. Single-cell Map of diverse immune phenotypes in the breast tumor microenvironment. Cell. 2018;174:1293–308.
42. Le K, Sun J, Ghaemmaghami J, Smith MR, Ip WKE, Phillips T, et al. Blockade of CCR1 induces a phenotypic shift in macrophages and triggers a favorable antilymphoma activity. Blood Adv. 2023;7:3952–67.
43. Liu X, Qin J, Nie J, Gao R, Hu S, Sun H, et al. ANGPTL2+cancer-associated fibroblasts and SPP1+macrophages are metastasis accelerators of colorectal cancer. Front Immunol. 2023;14:1185208.
44. Sathe A, Mason K, Grimes SM, Zhou Z, Lau BT, Bai X, et al. Colorectal cancer metastases in the liver establish immunosuppressive spatial networking between tumor-associated SPP1+ macrophages and fibroblasts. Clin Cancer Res. 2023;29:244–60.
45. Bill R, Wirapati P, Messemaker M, Roh W, Zitti B, Duval F, et al. CXCL9:SPP1 macrophage polarity identifies a network of cellular programs that control human cancers. Science. 2023;381:515–24.
46. Moon JW, Kong S, Kim BS, Kim HJ, Lim H, Noh K, et al. IFNgamma induces PD-L1 overexpression by JAK2/STAT1/IRF-1 signaling in EBV-positive gastric carcinoma. Sci Rep. 2017;7:17810.
47. Ivashkiv LB. IFNgamma: signalling, epigenetics and roles in immunity, metabolism, disease and cancer immunotherapy. Nat Rev Immunol. 2018;18:545–58.
48. Chang Q, Bournazou E, Sansone P, Berishaj M, Gao SP, Daly L, et al. The IL-6/JAK/Stat3 feed-forward loop drives tumorigenesis and metastasis. Neoplasia. 2013;15:848–62.
49. Kortylewski M, Xin H, Kujawski M, Lee H, Liu Y, Harris T, et al. Regulation of the IL-23 and IL-12 balance by Stat3 signaling in the tumor microenvironment. Cancer Cell. 2009;15:114–23.
50. Pathria P, Gotthardt D, Prchal-Murphy M, Putz E, Holcmann M, Schlederer M, et al. Myeloid STAT3 promotes formation of colitis-associated colorectal cancer in mice. Oncoimmunology. 2015;4:e998529.
51. Rahmani M, Nkwocha J, Hawkins E, Pei X, Parker RE, Kmieciak M, et al. Cotargeting BCL-2 and PI3K induces BAX-dependent mitochondrial apoptosis in AML cells. Cancer Res. 2018;78:3075–86.
52. Sahin E, Haubenwallner S, Kuttke M, Kollmann I, Halfmann A, Dohnal AM, et al. Macrophage PTEN regulates expression and secretion of arginase I modulating innate and adaptive immune responses. J Immunol. 2014;193:1717–27.
53. Kaneda MM, Messer KS, Ralainirina N, Li H, Leem CJ, Gorjestani S, et al. PI3Kgamma is a molecular switch that controls immune suppression. Nature. 2016;539:437–42.
54. Lian G, Chen S, Ouyang M, Li F, Chen L, Yang J. Colon cancer cell secrete EGF to promote M2 polarization of TAM through EGFR/PI3K/AKT/mTOR pathway. Technol Cancer Res Treat. 2019;18:1078116716.
55. Wu J, Jiang L, Wang S, Peng L, Zhang R, Liu ZTGF. beta1 promotes the polarization of M2-type macrophages and activates PI3K/mTOR signaling pathway by inhibiting ISG20 to sensitize ovarian cancer to cisplatin. Int Immunopharmacol. 2024;134:112235.
56. Cao LL, Kagan JC. Targeting innate immune pathways for cancer immunotherapy. Immunity. 2023;56:2206–17.
57. Zhang X, Liu X, Zhou W, Du Q, Yang M, Ding Y, et al. Blockade of IDO-kynurenine-AhR axis ameliorated colitis-associated colon cancer via inhibiting immune tolerance. Cell Mol Gastroenterol Hepatol. 2021;12:1179–99.
58. Hashimoto M, Kojima Y, Sakamoto T, Ozato Y, Nakano Y, Abe T, et al. Spatial and single-cell colocalisation analysis reveals MDK-mediated immunosuppressive environment with regulatory T cells in colorectal carcinogenesis. EBioMedicine. 2024;103:105102.
59. Mei Y, Xiao W, Hu H, Lu G, Chen L, Sun Z, et al. Single-cell analyses reveal a suppressive tumor microenvironment of human colorectal cancer. Clin Transl Med. 2021;11:e422.
60. Kersten K, Hu KH, Combes AJ, Samad B, Harwin T, Ray A, et al. Spatiotemporal co-dependency between macrophages and exhausted CD8(+) T cells in cancer. Cancer Cell. 2022;40:624–38.
61. Mazet JM, Mahale JN, Tong O, Watson RA, Lechuga-Vieco AV, Pirgova G, et al. IFNgamma signaling in cytotoxic T cells restricts anti-tumor responses by inhibiting the maintenance and diversity of intra-tumoral stem-like T cells. Nat Commun. 2023;14:321.
62. Omatsu M, Nakanishi Y, Iwane K, Aoyama N, Duran A, Muta Y, et al. THBS1-producing tumor-infiltrating monocyte-like cells contribute to immunosuppression and metastasis in colorectal cancer. Nat Commun. 2023;14:5534.
63. Natarajan A, Wagner B, Sibilia M. The EGF receptor is required for efficient liver regeneration. Proc Natl Acad Sci USA. 2007;104:17081–6.
64. Clausen BE, Burkhardt C, Reith W, Renkawitz R, Förster I. Conditional gene targeting in macrophages and granulocytes using LysMcre mice. Transgenic Res. 1999;8:265–77.
65. Caton ML, Smith-Raska MR, Reizis B. Notch-RBP-J signaling controls the homeostasis of CD8- dendritic cells in the spleen. J Exp Med. 2007;204:1653–64.
66. Zhang X, Goncalves R, Mosser DM. The isolation and characterization of murine macrophages. Curr Protoc Immunol. 2008;Chapter 14:11–4.
67. Linder M, Glitzner E, Srivatsa S, Bakiri L, Matsuoka K, Shahrouzi P, et al. EGFR is required for FOS-dependent bone tumor development via RSK2/CREB signaling. EMBO Mol Med. 2018;10:e9408.
68. Barkas N, Petukhov V, Kharchenko P, Steiger S, Rydbirk R. Biederstedt E pagoda2: single cell analysis and differential expression. R package version 1.0.12. 2021.
69. Stuart T, Butler A, Hoffman P, Hafemeister C, Papalexi E, Mauck WMR, et al. Comprehensive integration of single-cell data. Cell. 2019;177:1888–902.
70. Becht E, McInnes L, Healy J, Dutertre C, Kwok IWH, Ng LG, et al. Dimensionality reduction for visualizing single-cell data using UMAP. Nat Biotechnol. 2019;37:38–44.
71. Ritchie ME, Phipson B, Wu D, Hu Y, Law CW, Shi W, et al. limma powers differential expression analyses for RNA-sequencing and microarray studies. Nucleic Acids Res. 2015;43:e47.
72. Hochberg Y, Benjamini Y. More powerful procedures for multiple significance testing. Stat Med. 1990;9:811–8.
73. Hanzelmann S, Castelo R, Guinney J. GSVA: gene set variation analysis for microarray and RNA-seq data. BMC Bioinforma. 2013;14:7.
74. Liberzon A, Birger C, Thorvaldsdottir H, Ghandi M, Mesirov JP, Tamayo P. The Molecular Signatures Database (MSigDB) hallmark gene set collection. Cell Syst. 2015;1:417–25.
75. Muller T, Kalxdorf M, Longuespee R, Kazdal DN, Stenzinger A, Krijgsveld J. Automated sample preparation with SP3 for low-input clinical proteomics. Mol Syst Biol. 2020;16:e9111.
76. Galaxy Community. The Galaxy platform for accessible, reproducible, and collaborative data analyses: 2024 update. Nucleic Acids Res. 2024;52:W83–94.

77. Law CW, Chen Y, Shi W, Smyth GK. voom: Precision weights unlock linear model analysis tools for RNA-seq read counts. Genome Biol. 2014;15:R29.
78. Lee J, Kim J, Chu HBK, Oh S, Kang S, Lee S, et al. Comprehensive RNA-sequencing analysis of colorectal cancer in a Korean cohort. Mol Cells. 2024;47:100033.
79. Roelands J, Kuppen PJK, Ahmed EI, Mall R, Masoodi T, Singh P, et al. An integrated tumor, immune and microbiome atlas of colon cancer. Nat Med. 2023;29:1273–86.
80. Viechtbauer W. Conducting Meta-Analyses in *R* with the metafor Package. J Stat Softw. 2010;36:1–48.

ACKNOWLEDGEMENTS

We would like to thank Martina Hammer and the staff of the Department of Biomedical Research of the Medical University of Vienna for the maintenance of the mouse colonies. We are grateful to Christine Tuppy, Marija Veljanoska and Luise Bellach for help with genotyping and to Alexandra Bogusch, Bilge Göcen-Oguz, Lilyana Mireva and Temenuschka Baykuscheva-Gentscheva for technical assistance. We thank the biomedical sequencing facility (BSF) of the Medical University of Vienna and the Center for Molecular Medicine of the Austrian Academy of Sciences for their assistance with scRNAseq. We are grateful to Michael Bergmann from the Department of General Surgery at the Medical University of Vienna for providing human CRC tissue sections. We also appreciate the excellent support of Gerald Timelthaler and Dominik Kirchhofer from the Microscopy & Imaging Facility, as well as the great help of the flow cytometry core facility of the Center for Cancer Research (Johannes Reisecker) and the Medical University of Vienna. We would like to thank Yu Yang from the Li Ka Shing Faculty of Medicine, University of Hong Kong, for statistical support with multivariate analysis. We thank Thomas Bauer for support with the graphical abstract.

AUTHOR CONTRIBUTIONS

MS conceptualized, designed and supervised the project and acquired the funding necessary for the whole study. OF, AN, and MH performed most of the wet lab experiments. TC performed most of the computational analysis. OF, TM, IB, DK, YX and BB helped with bioinformatic data analyses. MF was instrumental in the library preparation, providing important advice and experimental material. ML assisted with mouse experiments. DF, BH and UK performed the proteomic analyses. MF, IB, UK, and MH provided intellectual contributions, methodology, and/or reagents. OF, AN, and MH wrote the original draft together with MF and MS, and all the authors reviewed and edited it.

FUNDING

This work was supported by grants acquired by MS: the European Research Council (ERC) Advanced grant (ERC-2015 AdG TNT-Tumors 694883), the European Union's Horizon 2020 research and innovation program under the Marie Skłodowska-Curie grant agreement No 766214 (META-CAN), the Austrian Science Fund FWF, DK-PhD program W1212 "Inflammation and Immunity" & DocFunds DOC 188 "SHIELD". DK was further supported by the Fellinger Cancer Research Fund and the City of Vienna Fund for Innovative Interdisciplinary Cancer Research. The work of AN was further supported by a grant from the Comprehensive Cancer Center. MF was supported by a special research grant (SFB) of the Austrian Science Fund (FWF) – SFB-F6103. The work of the UK was supported by the European Union's Horizon Europe program (FOR 5146) through the ERC network ARTEMIS (grant agreement No. 101136299). Additional support to the UK was provided by the German Ministry for Education and Research (BMBF) through the German Center for Lung Research (DZL 3.0: 82DZL004B4; DZL 4.0: 82DZL004C4), the MSCoreSys networks SMART-CARE (031L0212B) and SMART-CARE2 (16LW0234), as well as the LiSyM-Cancer networks SMART-NAFLD (031L0256A) and C-TIP-HCC (031L0257C). Open access funding provided by Medical University of Vienna.

COMPETING INTERESTS

The authors declare no competing interests.

ETHICS APPROVAL

Mice were bred and maintained in the animal facilities of the Medical University of Vienna in accordance with institutional policies and federal guidelines. Animal experiments conducted were approved by the Animal Experimental Ethics Committee of the Medical University of Vienna and the Austrian Federal Ministry of Science and Research (animal license number BMBWF-66.009/0369-V/3b/2019). Human CRC material was obtained from the Department of General Surgery at the Medical University of Vienna (Ethics approval ID 1580/2017). Informed consent was obtained from all subjects.

ADDITIONAL INFORMATION

Supplementary information The online version contains supplementary material available at https://doi.org/10.1038/s41418-026-01774-x.

Correspondence and requests for materials should be addressed to Maria Sibilia.

Reprints and permission information is available at http://www.nature.com/reprints

Publisher's note Springer Nature remains neutral with regard to jurisdictional claims in published maps and institutional affiliations.

Open Access This article is licensed under a Creative Commons Attribution 4.0 International License, which permits use, sharing, adaptation, distribution and reproduction in any medium or format, as long as you give appropriate credit to the original author(s) and the source, provide a link to the Creative Commons licence, and indicate if changes were made. The images or other third party material in this article are included in the article's Creative Commons licence, unless indicated otherwise in a credit line to the material. If material is not included in the article's Creative Commons licence and your intended use is not permitted by statutory regulation or exceeds the permitted use, you will need to obtain permission directly from the copyright holder. To view a copy of this licence, visit http://creativecommons.org/licenses/by/4.0/.

© The Author(s) 2026